J. Fluid Mech. (2001), *vol.* 430, *pp.* 231–265. Printed in the United Kingdom

Prandtl–Meyer flows with homogeneous condensation. Part 2. Supercritical flows

By C. F. DELALE[1] AND D. G. CRIGHTON[2]†

[1]TÜBİTAK Feza Gürsey Institute, PO Box 6, 81220 Çengelköy, Istanbul, Turkey

[2]Department of Applied Mathematics and Theoretical Physics
University of Cambridge, Silver Street, Cambridge CB3 9EW, UK

(Received 14 February 2000 and in revised form 3 October 2000)

Prandtl–Meyer flows with embedded oblique shock waves due to excessive heat release from condensation (*supercritical flows*) are considered by extending the subcritical asymptotic solution of Delale & Crighton (1998). The embedded shock origin is located by the construction of the envelope of the family of characteristics emanating either from the corner or from the deflected wall in the parabolic approximation. A shock fitting technique for embedded oblique shock waves is introduced in the small deflection angle approximation and the law of deflection of a streamline through an embedded oblique shock wave is established within the same approximation. The network of characteristics downstream of the embedded shock front is constructed and the solution for the flow field therein is evaluated by utilizing the asymptotic solution of the rate equation along streamlines downstream of the shock front together with the equations of motion in characteristic form. Results obtained by employing the classical nucleation equation and the Hertz–Knudsen droplet growth law, compared with the supercritical experiments of Smith (1971) for moist air expansions, show that supercritical Prandtl–Meyer flows can only be realized locally when the embedded shock lies sufficiently far downstream of the throat, where the corner is located.

1. Introduction

Prandtl–Meyer flows with homogeneous condensation are of considerable interest in the physical sciences and in technology. They have direct applications at the trailing edge of the blades in steam turbines and can affect the downstream wake structure. The subject has been investigated both experimentally and theoretically by Smith (1971), Kurshakov, Saltanov & Tkalenko (1971) and Frank (1979, 1985). An asymptotic solution of the problem for subcritical flows (flows without embedded shock waves) was recently given in Part 1 (Delale & Crighton 1998 and references therein). Results obtained for Smith's experiments by this asymptotic solution showed intersecting characteristics in the heat addition zones, clearly exhibiting the need to incorporate embedded shock waves due to excessive heat release from condensation (*supercritical flows*). A qualitative theory recently developed by Delale & van Dongen (1998) show that such shock waves are weak. Supercritical Prandtl–Meyer flows have never been calculated, mainly due to the lack of a shock fitting technique for embedded weak oblique shock waves in non-uniform flows. The computation of the

† Professor Crighton died during the publication process of this paper in April 2000.

near-corner solution, where intense heat release to the flow occurs, presents another major difficulty. This investigation is devoted to the resolution of these difficulties.

In this investigation a method of computation of supercritical Prandtl–Meyer flows with embedded weak oblique shock waves, due to intense heat release from condensation, is presented. Shock formation theory is discussed and the embedded shock origin is located by the envelope of the family of intersecting characteristics in the parabolic approximation. A shock fitting technique for embedded oblique shock waves is introduced in the small deflection angle approximation. Consequently, the law of deflection of a streamline through an embedded oblique shock wave is established in this approximation. The network of characteristics downstream of the shock is constructed and the flow field therein is evaluated using the asymptotic solution of the condensation rate equation along streamlines in different regimes downstream of the shock front. A supercritical algorithm for such a flow field is developed incorporating the embedded oblique shock relations and is applied to the experiments of Smith (1971). The results show that Prandtl–Meyer flows can only be realized with an embedded oblique shock wave downstream of the nozzle throat where the corner is located. Embedded shock waves near the throat show strong shock behaviour with subsonic flow field behind (e.g. see also Frank 1985), similar to those observed in ducts and nozzles, and cannot be calculated by the theory developed here for supercritical Prandtl–Meyer flows.

2. Equations of motion and asymptotic solution of the condensation rate equation for supercritical flows

We consider the steady two-dimensional equations of motion of a mixture of a condensable vapour and a carrier gas in natural coordinates and normalized form:

$$\frac{1}{\rho}\frac{\partial \rho}{\partial s} + \frac{1}{u}\frac{\partial u}{\partial s} - \frac{\partial \theta}{\partial n} = 0, \tag{1}$$

$$\rho u \frac{\partial u}{\partial s} = -\frac{\partial p}{\partial s}, \tag{2}$$

$$\rho u^2 \frac{\partial \theta}{\partial s} = \frac{\partial p}{\partial n}, \tag{3}$$

$$\rho \frac{\partial h}{\partial s} = \frac{\partial p}{\partial s}, \tag{4}$$

and

$$p = \left(1 - \frac{\mu_m}{\mu_v} g\right) \rho T \tag{5}$$

where s and n are the normalized streamwise and normal coordinates, ρ, p, u and T are, respectively, the normalized mixture density, pressure, flow speed and temperature, θ is the flow angle, g is the condensate mass fraction; and h is the normalized mixture enthalpy given by

$$h = c_{pm} T - \frac{\mu_m}{\mu_v} g L(T), \tag{6}$$

with c_{pm} denoting the normalized mixture specific heat at constant pressure, L the latent heat of condensation and μ_m and μ_v, respectively, the molecular weights of the mixture and of the condensable vapour. (For normalization and other details, see

Part 1. Note that in equations (20) and (39) of Part 1, the missing factor μ_m/μ_v, that multiplies the term $g\,L$, should be included.)

The flow and state equations (1)–(6) should be supplemented by the condensation rate equation

$$g(s) = \int_{s_c}^{s} [r^*(\xi) + \lambda \int_{\xi}^{s} \Omega(\eta)\,\mathrm{d}\eta]^3 \frac{\Sigma(\xi)}{\rho(\xi)\,u(\xi)} \exp\,[-K^{-1}B(\xi)]\,\mathrm{d}\xi \tag{7}$$

along streamlines constructed from a normalized nucleation equation

$$J = \Sigma(p, T, g) \exp\,[-K^{-1}B(p, T, g)] \tag{8}$$

and a normalized radius-independent droplet growth law

$$\frac{\partial r}{\partial s} = \lambda\Omega(p, T, g), \tag{9}$$

with details given in Part 1. In (7)–(9) B, Ω and Σ, respectively, denote the normalized activation function, the normalized droplet growth function and the pre-exponential factor of nucleation, K is the nucleation parameter (assumed to be small compared to unity), λ is the droplet growth parameter and r^* is the normalized critical radius beyond which condensation nuclei grow into droplets.

A continuous solution of (1)–(9) for Prandtl–Meyer flows is given in Part 1, using the asymptotic solution of the condensation rate equation (7) along streamlines. This solution is valid only if the characteristics or Mach lines emanating from the corner or the deflected wall do not intersect in the heat addition zones. When these characteristics intersect, which seems to be typical for most condensing Prandtl–Meyer flows that can be experimentally realized, embedded oblique shock waves appear to redirect the flow diverted by excessive heat release from condensation. Such flows will be called *supercritical* in contrast to subcritical flows where the flow field is everywhere continuous in the domain of interest. Figure 1 shows a typical supercritical flow with an embedded shock front KL due to excessive heat release by condensation. It has been demonstrated by Delale & van Dongen (1998) that such a shock wave shows a supersonic to supersonic transition and can, therefore, be assumed to be weak (strong shock waves with supersonic to subsonic transition occur in supercritical flows in ducts and nozzles, e.g. see Schnerr (1989) and Delale, Schnerr & Zierep (1993*a*, *b*)). The existence of an embedded shock KL, with a portion KG lying in the heat addition zones and with a portion GL lying in the nearly frozen zones, distinguishes the different classes of streamlines, designated *a* to *e* in figure 1, which have distinct condensation zones according to the variation of the normalized activation function B along them. Figure 2(*a*–*e*) classifies the possible variations of B along streamlines for these classes. Figure 2(*a*) shows the condensation zones along a typical streamline of class *a* in figure 1, as encountered in subcritical Prandtl–Meyer flows. In this case the condensation zones (initial growth zone IGZ, further growth zone FGZ, rapid growth zone RGZ, onset zone OZ, nucleation zone with growth NZ and droplet growth zone DGZ) are precisely the same as those given in Part 1. Figure 2(*b*–*e*), on the other hand, shows the condensation zones and variation of B along streamlines of those classes which pass through the embedded shock wave KL. In particular figures 2(*b*) and 2(*c*) show the condensation zones along streamlines *b* and *c* in figure 1, which pass through the portion KG of the embedded shock in the heat addition zones whereas figures 2(*d*) and 2(*e*) show the condensation zones along streamlines *d* and *e* in figure 1, which pass through the portion GL of the embedded shock in the nearly frozen zones. The embedded shock location s_z along

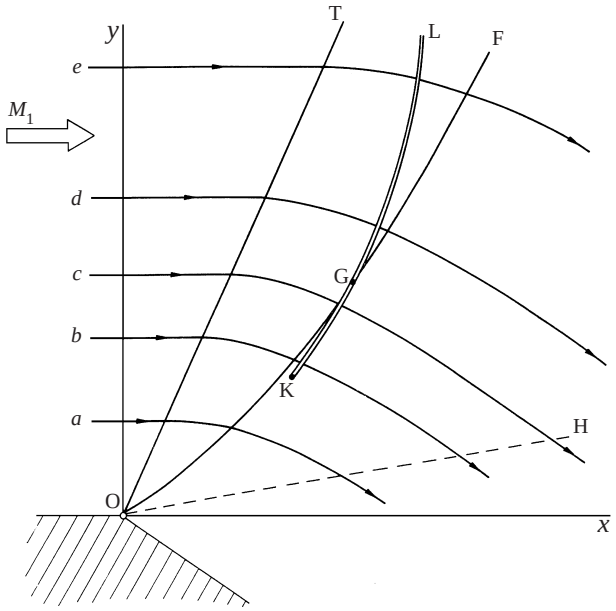

FIGURE 1. Different classes of streamlines in Prandtl–Meyer flows with an embedded oblique shock wave KGL (OT and OH are, respectively, the isentropic tail and head of the expansion fan and OGF is the subcritical nucleation wave front). *a*, A typical streamline which does not intersect the shock front, therefore along which the flow field remains subcritical; *b*, a typical streamline which intersects the shock front in the droplet growth zone (DGZ); *c*, a typical streamline which intersects the shock front in the nucleation zone with growth (NZ); *d*, a typical streamline which intersects the shock front in the rapid growth zone (RGZ); and *e*, a typical streamline which intersects the shock front in the further growth zone (FGZ).

each streamline *b*–*e* in figure 1, lies, respectively, in the droplet growth zone DGZ, in the nucleation zone with growth NZ, in the rapid growth zone RGZ and in the further growth zone FGZ. The onset zone OZ, in which the observed onset of condensation falls, precedes the embedded shock location s_z in each case, as seen in figure 2(*b*–*e*).

The condensation rate equation (7) and its asymptotic solution presented in Part 1 remain valid only on streamlines *a*, which are typical for subcritical flows. For supercritical flows, which are observed on streamlines *b*–*e* of figure 1, the condensation rate equation and its asymptotic solution have to be reconsidered in each case. In reformulating the condensation rate equation along streamlines, the thermodynamic functions r^*, B, Σ and Ω of Part 1 (see also (7)) are taken to be piecewise smooth functions of the three independent thermodynamic coordinates p, T and g. Across the embedded oblique shock, the pressure p and temperature T are discontinuous in spite of the fact that the jumps in these variables may turn out to be small. Consequently, the thermodynamic functions r^*, B, Σ, Ω and L exhibit discontinuities at the embedded shock location s_z along streamlines. We use an overbar to denote the thermodynamic functions in domain $s > s_z$ along streamlines to distinguish them from those in domain $s < s_z$. We denote by subscript a all thermodynamic functions as $s \to s_z^-$ and by subscript b all thermodynamic functions as $s \to s_z^+$ (e.g. $B_a = \lim_{s \to s_z^-} B(s)$ and $B_b = \lim_{s \to s_z^+} \bar{B}(s)$; also note that $B_a \neq B_b$) along streamlines. The condensation rate equation (7) remains valid along streamlines *b*–*e* of figure 1 for $s \leqslant s_z$ only. For

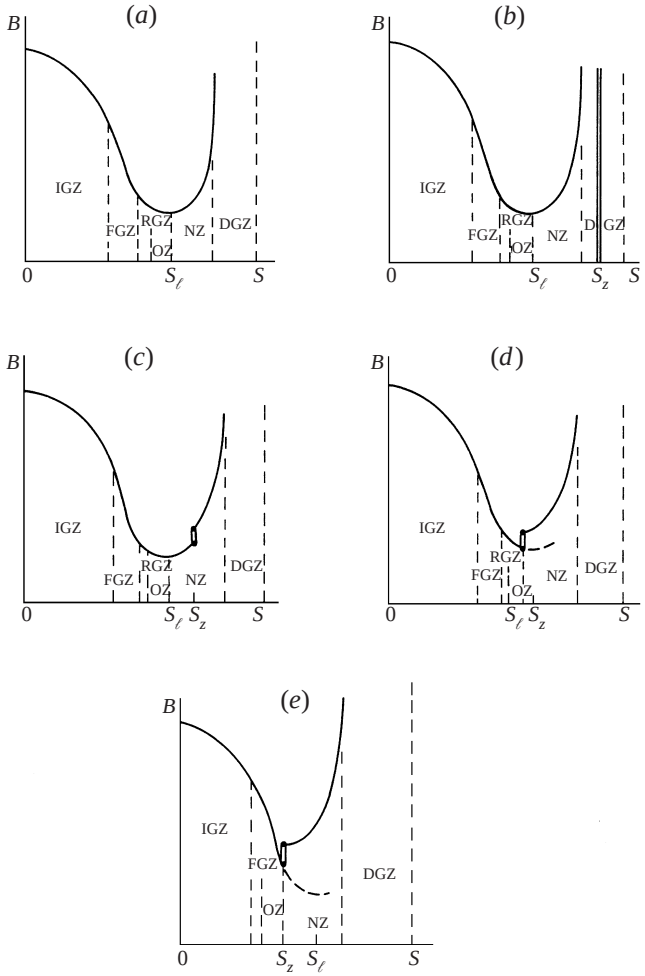

FIGURE 2. The variation of the normalized activation function B versus s along streamlines of different classes (IGZ is the initial growth zone, FGZ is the further growth zone, RGZ is the rapid growth zone, OZ is the onset zone, NZ is the nucleation zone with growth, DGZ is the droplet growth zone, s is the streamwise coordinate, s_z is the location of the shock front on the streamline, and s_ℓ is the location of the turning point of B in subcritical flows): (*a*) in subcritical flows, (*b*) s_z lies in DGZ, (*c*) s_z lies in NZ, (*d*) s_z lies in RGZ, and (*e*) s_z lies in FGZ.

$s \geqslant s_z$, the condensation rate equation can be written as

$$g(s) = \int_{s_c}^{s_z} \left[r^*(\xi) + \lambda \int_{\xi}^{s_z} \Omega(\eta)\,\mathrm{d}\eta + \lambda \int_{s_z}^{s} \bar{\Omega}(\eta)\,\mathrm{d}\eta \right]^3 \frac{\Sigma(\xi)}{\rho(\xi)\,u(\xi)} \exp\left[-K^{-1}B(\xi)\right]\mathrm{d}\xi$$
$$+ \int_{s_z}^{s} \left[\bar{r}^*(\xi) + \lambda \int_{\xi}^{s} \bar{\Omega}(\eta)\,\mathrm{d}\eta \right]^3 \frac{\bar{\Sigma}(\xi)}{\bar{\rho}(\xi)\,\bar{u}(\xi)} \exp\left[-K^{-1}\,\bar{B}(\xi)\right]\mathrm{d}\xi. \tag{10}$$

In (10) the first integral characterizes the contribution from nuclei created upstream of the shock location whereas the second integral characterizes the contribution from nuclei produced downstream of the shock location. It can readily be observed from (7) and (10) that the condensate mass fraction g is continuous at $s = s_z$ along streamlines; however, its derivative is discontinuous at the shock location. Differentiating (7) and

(10) with respect to s along streamlines, we have for $s < s_z$

$$\frac{\partial g}{\partial s} = r^{*3}(s)\frac{\Sigma(s)}{\rho(s)\,u(s)}\exp\left[-K^{-1}B(s)\right] + 3\lambda\Omega(s)\int_{s_c}^{s}\left[r^{*}(\xi)+\lambda\int_{\xi}^{s}\Omega(\eta)\,\mathrm{d}\eta\right]^{2}\frac{\Sigma(\xi)}{\rho(\xi)\,u(\xi)}\exp\left[-K^{-1}B(\xi)\right]\mathrm{d}\xi \quad (11)$$

and for $s > s_z$

$$\frac{\partial g}{\partial s} = \bar{r}^{*3}(s)\,\frac{\bar{\Sigma}(s)}{\bar{\rho}(s)\,\bar{u}(s)}\exp\left[-K^{-1}\bar{B}(s)\right] + 3\lambda\bar{\Omega}(s)\int_{s_c}^{s_z}\left[r^{*}(\xi)+\lambda\int_{\xi}^{s_z}\Omega(\eta)\,\mathrm{d}\eta+\lambda\int_{s_z}^{s}\bar{\Omega}(\eta)\,\mathrm{d}\eta\right]^{2} \times\frac{\Sigma(\xi)}{\rho(\xi)\,u(\xi)}\exp\left[-K^{-1}B(\xi)\right]\mathrm{d}\xi + 3\lambda\bar{\Omega}(s)\int_{s_z}^{s}\left[\bar{r}^{*}(\xi)+\lambda\int_{\xi}^{s}\bar{\Omega}(\eta)\,\mathrm{d}\eta\right]^{2}\frac{\bar{\Sigma}(\xi)}{\bar{\rho}(\xi)\,\bar{u}(\xi)}\exp\left[-K^{-1}\bar{B}(\xi)\right]\mathrm{d}\xi. \quad (12)$$

Now by taking the limits $s \to s_z^-$ in (11) and $s \to s_z^+$ in (12), we obtain the shock condition for $\partial g/\partial s$ as

$$\left(\frac{\partial g}{\partial s}\right)_b = \frac{\Omega_b}{\Omega_a}\left(\frac{\partial g}{\partial s}\right)_a + r_b^{*3}\frac{\Sigma_b}{\rho_b\,u_b}\exp\left[-K^{-1}B_b\right] - \frac{\Omega_b}{\Omega_a}\,r_a^{*3}\frac{\Sigma_a}{\rho_a\,u_a}\exp\left[-K^{-1}B_a\right] \quad (13)$$

along streamlines c–e of figure 1. For typical streamlines of class b in figure 1 where $B_a = B_b \to \infty$, (13) reduces to

$$\left(\frac{\partial g}{\partial s}\right)_b = \frac{\Omega_b}{\Omega_a}\left(\frac{\partial g}{\partial s}\right)_a. \quad (14)$$

The asymptotic solutions of the condensation rate equation (7) and of its derivative, (11), of Part 1 remain valid along streamlines intersecting the shock front only in regions which lie upstream of it. The asymptotic solution of the rate equation along streamlines b–e in figure 1 downstream of the oblique shock location can be obtained from those given in Appendices A–D of Delale *et al.* (1993*b*) for supercritical nozzle flows. We use for the class b streamline of figure 1 the asymptotic solution downstream of the shock in regime IV in Appendix D, and for classes c, d and e, respectively, the corresponding solutions of regimes III, II and I given in Appendices C, B and A of Delale *et al.* (1993*b*) with the following modifications. The nozzle axial coordinate x should be replaced by the streamwise coordinate s, the normal shock location z along the nozzle axis should be replaced by the oblique shock location s_z along streamlines, the derivatives $\mathrm{d}/\mathrm{d}x$ and $\mathrm{d}^2/\mathrm{d}x^2$ along the nozzle axis should be replaced, respectively, by $\mathrm{d}/\mathrm{d}s$ and $\mathrm{d}^2/\mathrm{d}s^2$ along streamlines, subscripts $-$ and $+$ should be replaced, respectively, by subscripts a and b, the function Ω_2 should be replaced by the function $\bar{\Omega}$, and, finally, the normal area A_z in supercritical nozzle flows should be replaced by $1/(\rho_a\,u_a)$ for quantities evaluated just upstream of the oblique shock front and by $1/(\rho_b\,u_b)$ for quantities evaluated just downstream of the oblique shock front. Since these expressions for the supercritical asymptotic solution of the condensation rate equation along streamlines downstream of the oblique shock are lengthy and

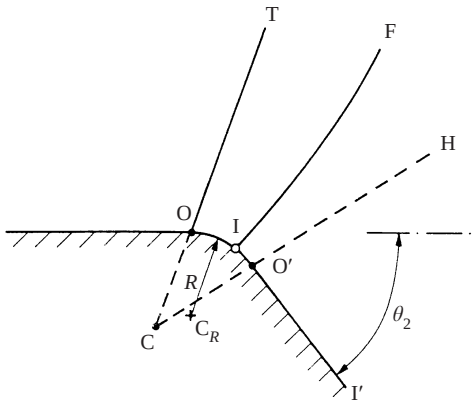

FIGURE 3. Position of the subcritical nucleation wave front IF with respect to the tail O′H of the expansion fan, centred at C and obtained by connecting two plane walls, deflected by an angle θ_2, by a circular arc OO′ with radius R and centre at C_R.

complicated, we do not present them here, but refer the reader to Delale *et al.* (1993*b*) with the modifications mentioned above.

3. Formation of embedded shock waves by homogeneous condensation

The heat release from condensation causes compressive effects along streamlines in the expansion fan of corner expansion flows resulting in the characteristics or Mach lines emanating from the corner and/or from the deflected wall approaching one another. As the heat release in the heat addition zones exceeds a critical value, these characteristics intersect, ruling out the possibility of a continuous solution. An embedded frozen oblique shock wave (curve KL in figure 1) then appears to redirect a flow diverted by excessive heat release. The computation of such flows (supercritical flows) requires a precise determination of the embedded shock origin K and the location of the embedded shock front KL of figure 1. In this section we determine the embedded shock origin K by the envelope construction of different possible families of intersecting characteristics. For this reason we search for possible flow patterns which exhibit different families of intersecting characteristics for corner expansion flows with embedded shock waves due to condensation. We consider two plane walls, with an angle θ_2 in between, connected by a circular arc OO′ with a normalized radius R and with centre at C_R, as shown in figure 3. In this case the centre C of the expansion fan and C_R of the arc OO′ are distinct points. The position of the subcritical nucleation wave front IF with respect to the expansion fan is also shown in figure 3. For corner expansion flows we let $R \to 0$ (the points O, O′, I, C and C_R then all coincide at the corner), and we obtain the possible families of characteristics, as shown in figure 4. As mentioned earlier these families of characteristics emanate either from the corner or from the deflected wall. In what follows we discuss shock formation theory by constructing the envelopes of the families of intersecting characteristics for each of the possibilities shown in figure 4.

3.1. *Equations of characteristics in the heat addition zones and existence of embedded shock waves*

We discuss the parametrization of the characteristic equations in the heat addition zones using figure 4. Using inviscid theory (neglecting boundary layers, wakes, etc.),

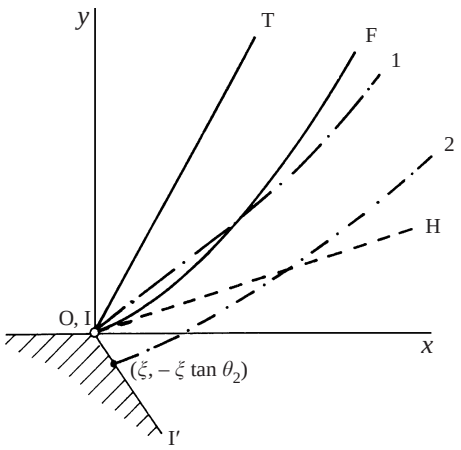

FIGURE 4. Classification of characteristics emanating either from the corner O or from the deflected wall OI′ in the physical plane. OT and OH are, respectively, the isentropic tail and head of the expansion fan, OF denotes the subcritical nucleation wave front, and 1 and 2 show typical characteristics of the same family, but with different parametrization, emanating either from the corner or from the deflected wall.

the solid wall is assumed to represent an isentropic streamline with a geometric singularity at the corner O. The point I, where the nucleation wave front meets the corner, is also a singular point. Thus, the geometric singularity O (the corner) and the physical singularity I coincide. Moreover, since heat release is always delayed with respect to nucleation, the nucleation wave front IF should meet the corner O at the slope of the isentropic wave head m_H. With this in mind, we discuss the parametrization of the characteristics in figure 4. Here, we can distinguish two types of characteristics, designated 1 and 2 in the heat addition zones. The characteristics of type 1 emanate from the corner O and are curved due to heat addition as they cross the nucleation wave front IF. We let m denote the initial slope of a characteristic line emanating from the corner and write the parametric equations of the nucleation wave front as

$$x_\ell = x_\ell(m) \qquad \text{and} \qquad y_\ell = y_\ell(m) \tag{15}$$

for $m_H \leqslant m \leqslant m_T$ where m_T and m_H are, respectively, the initial slopes of the isentropic wave tail and of the isentropic wave head. In this case the characteristics of type 1 emanating from the corner remain straight up to the nucleation wave front IF and are given by

$$y = m\,x \tag{16}$$

for $0 \leqslant x \leqslant x_\ell(m)$ and $m_H \leqslant m \leqslant m_T$. As the characteristics of type 1 of figure 4 traverse the nucleation wave front and enter the heat addition zones, they are curved due to substantial heat addition by condensation. In the first approximation these characteristics can be assumed to take the parabolic form

$$y = A(m)[x - x_\ell(m)]^2 + m\,x \tag{17}$$

for $x \geqslant x_\ell(m)$ and $m_H \leqslant m \leqslant m_T$ where the function $A(m)$ can be thought of as a measure of the curvature of a characteristic line with initial slope m in the heat addition zones. In particular, as $A(m) \to 0$ (negligible heat addition), the characteristics given by (17) become straight, as in the case of isentropic flow. It can be shown that

the characteristics given by (17) intersect in the heat addition zones provided that

$$\left[2\,A(m)\,\frac{\mathrm{d}x_\ell}{\mathrm{d}m}-1\right]^2-4\,\frac{\mathrm{d}A}{\mathrm{d}m}\,x_\ell(m)\geqslant 0. \tag{18}$$

Equation (18) can, thus, be taken as the necessary and sufficient condition for the existence of embedded shock waves due to intersecting characteristics of type 1 in figure 4. We now discuss the characteristic family of type 2 shown in figure 4. These characteristics emanate from the deflected wall and, in the parabolic approximation, can be parametrized by

$$y=\hat{A}(\xi)\,(x-\xi)^2+m_H\,(x-\xi)-(\tan\theta_2)\,\xi \tag{19}$$

where $\xi\geqslant 0$ denotes the initial abcissa of the emerging characteristic and where the function $\hat{A}(\xi)$ is to be determined from the subcritical solution of Part 1 in the heat addition zones. In particular, we have $\hat{A}(0)=A(m_H)$. The condition for the intersection of these characteristics becomes

$$[\hat{A}(\xi)]^2+\frac{\mathrm{d}\hat{A}}{\mathrm{d}\xi}(m_H+\tan\theta_2)\geqslant 0. \tag{20}$$

3.2. *Envelope construction and location of the embedded shock origin*

The parametric equations of the envelope of the family of intersecting characteristics in the heat addition zones of figure 4, discussed in the previous section in the parabolic approximation, are given by

$$\frac{\partial y}{\partial m}=0\Rightarrow x=\bar{x}(m) \tag{21}$$

where y is given by (17) and

$$y=\bar{y}(m)=A(m)[\bar{x}(m)-x_\ell(m)]^2+m\,\bar{x}(m) \tag{22}$$

for characteristics of type 1, and

$$\frac{\partial y}{\partial \xi}=0\Rightarrow x=\hat{x}(\xi) \tag{23}$$

where y is given by (19) and

$$y=\hat{y}(\xi)=\hat{A}(\xi)[\hat{x}(\xi)-\xi]^2+m_H[\hat{x}(\xi)-\xi]-(\tan\theta_2)\xi \tag{24}$$

for characteristics of type 2 in figure 4. In particular, the functions $\bar{x}(m)$ and $\hat{x}(\xi)$ are given by

$$\bar{x}(m)=\begin{cases} x_\ell(m)+\dfrac{2A(m)\mathrm{d}x_\ell/\mathrm{d}m-1\pm\sqrt{\Delta(m)}}{2(\mathrm{d}A/\mathrm{d}m)} & \text{if } \dfrac{\mathrm{d}A}{\mathrm{d}m}\neq 0 \\[2ex] x_\ell(m)+\dfrac{x_\ell(m)}{2A(m)\mathrm{d}x_\ell/\mathrm{d}m-1} & \text{if } \dfrac{\mathrm{d}A}{\mathrm{d}m}=0 \end{cases} \tag{25}$$

for $m_H\leqslant m<m_T$ and

$$\hat{x}(\xi)=\begin{cases} \xi+\dfrac{\hat{A}(\xi)\pm\sqrt{\hat{\Delta}(\xi)}}{\mathrm{d}\hat{A}/\mathrm{d}\xi} & \text{if } \dfrac{\mathrm{d}\hat{A}}{\mathrm{d}\xi}\neq 0 \\[2ex] \xi-\dfrac{(m_H+\tan\theta_2)}{2\hat{A}(\xi)} & \text{if } \dfrac{\mathrm{d}\hat{A}}{\mathrm{d}\xi}=0 \end{cases} \tag{26}$$

for $\xi \geqslant 0$ with

$$\Delta(m) = \left[2A(m)\frac{\mathrm{d}x_\ell}{\mathrm{d}m} - 1\right]^2 - 4\,\frac{\mathrm{d}A}{\mathrm{d}m}\,x_\ell(m) \geqslant 0 \tag{27}$$

and

$$\hat{\Delta}(\xi) = \left[\hat{A}(\xi)\right]^2 + \frac{\mathrm{d}\hat{A}}{\mathrm{d}\xi}\,(m_H + \tan\theta_2) \geqslant 0. \tag{28}$$

The positive definiteness of the functions $\Delta(m)$ and $\hat{\Delta}(\xi)$ follows from the conditions of intersecting characteristics given, respectively, by (18) and (20). The origin K of the embedded shock wave, in principle, can lie on the envelope of the family of characteristics of type 1 or 2 of figure 4. In either case the origin K is identified as the point where the discriminant of the quadratic equation for the coordinates of the envelope of each family vanishes. For the envelope of the intersecting characteristics of type 1 in figure 4, it follows from (21) that the embedded shock origin lies on a characteristic emerging from the corner with slope m_K given by the condition

$$\Delta(m_K) = 0 \tag{29}$$

where $\Delta(m)$ is given by (27). In this case the coordinates of the embedded shock origin K are given by

$$x_K = x_\ell(m_K) + \frac{\left(2\,A(m_K)\,(\mathrm{d}x_\ell/\mathrm{d}m)_K - 1\right)}{2\,(\mathrm{d}A/\mathrm{d}m)_K} \tag{30}$$

and

$$y_K = A(m_K)[x_K - x_\ell(m_K)]^2 + m_K\,x_K \tag{31}$$

where subscript K in the derivatives with respect to m denotes evaluation at $m = m_K$. On the other hand, if the embedded shock origin K lies on the envelope of intersecting characteristics emerging from the deflected wall, the initial x-coordinate ξ_K of the characteristic on which K lies can be obtained from the condition

$$\hat{\Delta}(\xi_K) = 0 \tag{32}$$

where $\hat{\Delta}(\xi)$ is given by (28). In this case the coordinates of the embedded shock origin K are

$$\hat{x}_K = \xi_K + \frac{\hat{A}(\xi_K)}{(\mathrm{d}\hat{A}/\mathrm{d}\xi)_K} \tag{33}$$

and

$$\hat{y}_K = \hat{A}(\xi_K)\left[\frac{\hat{A}(\xi_K)}{(\mathrm{d}\hat{A}/\mathrm{d}\xi)_K}\right]^2 + m_H\,\frac{\hat{A}(\xi_K)}{(\mathrm{d}\hat{A}/\mathrm{d}\xi)_K} - (\tan\theta_2)\,\xi_K. \tag{34}$$

It is now clear that the embedded shock origin K either lies on a characteristic emanating from the corner O with coordinates given by (30) and (31), or on a characteristic emanating from the deflected wall with coordinates given by (33) and (34). In the latter case the heat addition to the flow would be less than that of the former case.

For completeness, we would also like to mention the case of shock formation due to condensation for the expansion into vacuum as shown in figure 5. In this case only characteristics emanating from the corner, labelled 1 in figure 5, can be distinguished. Shock formation theory then follows the same lines of analysis as for the characteristics of type 1 of figure 4 treated above in detail.

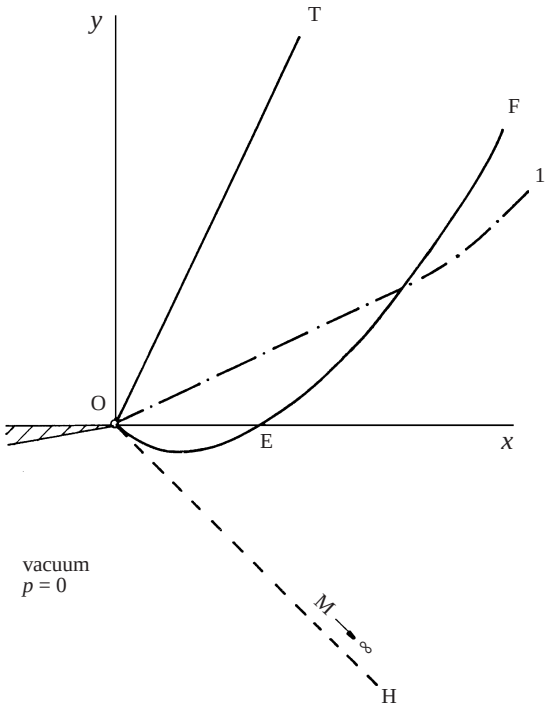

FIGURE 5. Classification of characteristics for the case of expansion into vacuum (OT and OH are, respectively, the isentropic tail and head of the expansion fan, OEF is the subcritical nucleation wave front, and 1 shows a typical characteristic of the family emanating from the corner O).

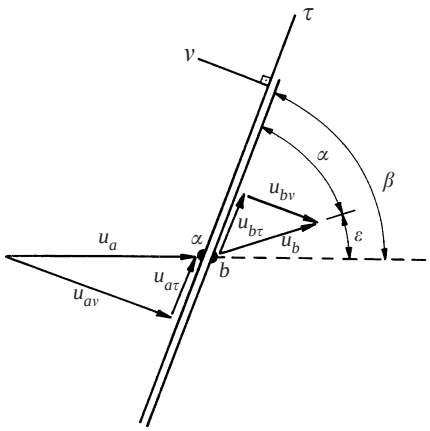

FIGURE 6. Geometry of an oblique shock wave (subscripts a and b denote, respectively, variables just ahead of and behind the shock front, subscripts v and τ denote, respectively, the normal and tangential components with respect to the shock front, β is the shock angle and ε is the angle of deflection of a streamline by the oblique shock).

3.3. *A model for the near-corner solution*

The above considerations for shock formation by homogeneous condensation require the determination of the nucleation wave front $x_\ell(m)$ and of the heat functions $A(m)$ and $\hat{A}(\xi)$ from the subcritical asymptotic solution of Part 1. Since heat addition to

the flow intensifies as the corner is approached due to high expansion rates, the near-corner subcritical asymptotic solution plays a dominant role in determining the heat functions and the nucleation wave front. It is important to mention that the expansion rate $\mathrm{d}T/\mathrm{d}s \to -\infty$ at the corner. Thus, the question of the validity of the subcritical asymptotic solution of Part 1 in the immediate neighbourhood of the corner arises. Indeed, for extremely high expansion rates, the distinct condensation zones along streamlines approach each other so rapidly that it is not possible to evaluate the asymptotic expressions near and beyond the nucleation wave front. Moreover, as the corner is approached, boundary layer, flow separation and heat transfer effects have to be considered. The physical mechanisms of condensation, i.e. nucleation and droplet growth theories, need to be revisited as well. For example, the very high expansion rates near the corner suggest that unsteady effects of nucleation have to be considered (see Delale & Schnerr 1996). In summary, the physical model employed needs to be modified to include the various complex phenomena mentioned above. Even if such a task could be fulfilled, giving a very complicated model, it would be very improbable that a satisfactory solution to the problem could be obtained by any means. In this paper we will approach the corner along streamlines as long as the subcritical asymptotic algorithm of Part 1 remains valid, without the complex phenomena mentioned above. We will then extrapolate the heat function and the subcritical nucleation wave front to regions near the corner. In doing so, we recommend polynomial extrapolation for the function $x_\ell(m)$, obtained in regions near the corner where the subcritical asymptotic algorithm of Part 1 applies. For the extrapolation of the heat function, one has to first choose one of the cases discussed for shock formation. Let us assume that the embedded shock origin lies on a characteristic of the family given by (16) and (17) where the heat function $A(m)$ is to be determined. We first note that $A(m) \geqslant 0$ for $m_H \leqslant m \leqslant m_T$ since the characteristics are concave upward in the heat addition zones. As $m \to m_T$, we have isentropic flow; therefore, $A(m) \to 0$. Also, as $m \to m_H$, for sufficiently large distances away from the wall, we have complete relaxation to equilibrium flow with negligible latent heat addition along streamlines so that $A(m) \to 0$ again. Since $A(m)$ is presumably continuous in $[m_H, m_T]$ and differentiable in (m_H, m_T), it follows by Rolle's theorem that $\mathrm{d}A/\mathrm{d}m = 0$ for some $\bar{m}$ in (m_H, m_T). Since $A(m) \geqslant 0$, the heat function $A(m)$ exhibits a local maximum at $m = \bar{m}$. Moreover, near the corner, heat addition to the flow occurs in a more or less symmetric fashion along streamlines. Finally, as the corner is approached, the heat function $A(m)$ steepens with decreasing bandwidth. All of the above properties of the heat function can be taken into account by assuming a Gaussian distribution in the form

$$A(m) = \frac{1}{\sqrt{2\pi}\sigma} \exp\left[-\frac{(m-\bar{m})^2}{2\sigma^2}\right] \tag{35}$$

with $\bar{m}$ denoting the mean and σ denoting the standard deviation. This function has inflection points at $m_0 = \bar{m} \pm \sigma$. Thus, from the data to be found by the subcritical algorithm, one can find the best fit by least squares (it would be easier to guess either of m_0 or $\bar{m}$ from the data and perform a one-parameter fit instead of two). Then, one can find m_K from (29). The coordinates of the embedded shock origin follow from (30) and (31). If such a value of m_K cannot be found, one proceeds to evaluate $\hat{A}(\xi)$ in a similar fashion by a Gaussian fit and use (32) to evaluate ξ_K. The coordinates of the embedded shock origin can then be evaluated from (33) and (34).

4. Oblique shock relations for condensing flows

The oblique shock relations for condensing flows have already been discussed in detail by Clarke & Delale (1988). Here, we present these relations and their solution. We let subscripts a and b denote, respectively, the quantities just ahead of and behind the oblique shock wave as shown in figure 6. We also let subscript v denote the component normal to the shock front and subscript τ denote the component tangent to the shock front. If β is the shock angle, defined as the angle between u_a and the shock front, a deviation in the flow direction, by angle ε, occurs. Consequently, the angle α between u_b and the shock front will be $\alpha = \beta - \varepsilon$ (see figure 6). The conservation of mass, momentum and energy together with the thermal equation of state across the shock surface yield

$$\rho_a\, u_{av} = \rho_b\, u_{bv}, \tag{36}$$

$$p_a + \rho_a\, u_{av}^2 = p_b + \rho_b\, u_{bv}^2, \tag{37}$$

$$u_{a\tau} = u_{b\tau}, \tag{38}$$

$$c_{pm}\, T_a + \tfrac{1}{2}\, u_a^2 - \frac{\mu_m}{\mu_v}\, L(T_a)\, g^* = c_{pm}\, T_b + \tfrac{1}{2}\, u_b^2 - \frac{\mu_m}{\mu_v}\, L(T_b)\, g^* \tag{39}$$

and

$$\frac{p_a}{\rho_a\, T_a} = \frac{p_b}{\rho_b\, T_b} = 1 - \frac{\mu_m}{\mu_v}\, g^*, \tag{40}$$

where g^* is the frozen value of the condensate mass fraction at the shock front. We now, for convenience, define a Mach number by

$$M = \frac{u}{(\gamma\, T)^{1/2}} \tag{41}$$

where γ is the adiabatic exponent of the mixture defined by $\gamma \equiv c_{pm}/(c_{pm} - 1)$. This Mach number can be related to the flow Mach number M_g, based on the local frozen speed of sound a_f, by

$$M_g^2 \equiv \frac{u^2}{a_f^2} = M^2\, \frac{(c_{pm} - 1 + \mu_m/\mu_v\, g)}{(c_{pm} - 1)\,(1 - \mu_m/\mu_v\, g)}. \tag{42}$$

For values of the condensate mass fraction $g \ll 1$, as encountered for moist air expansions, we have $M \approx M_g$. Equations (36)–(41) yield the relations

$$\begin{aligned} M_{bv}^2 = \Bigg[& \frac{F(M_{av}^2)}{2\,(\gamma - 1)} - \gamma\, \left(1 - \frac{\mu_m}{\mu_v}\, g^*\right) \\ & \pm \left\{ \left[\frac{F(M_{av}^2)}{2\,(\gamma - 1)}\right]^2 - (1 - \frac{\mu_m}{\mu_v}\, g^*)\, \left[\frac{\gamma}{(\gamma - 1)} - \frac{1}{2}\, \left(1 - \frac{\mu_m}{\mu_v}\, g^*\right)\right] F(M_{av}^2) \right\}^{1/2} \Bigg] \\ & \times \left[\gamma^2 - \frac{F(M_{av}^2)}{2}\right]^{-1} \end{aligned} \tag{43}$$

where

$$F(M_{av}^2) = \frac{(1 - \mu_m/\mu_v\, g^* + \gamma\, M_{av}^2)}{[1/(\gamma - 1) - (\mu_m/\mu_v)\, \Delta L\, g^*/(\gamma\, T_a)]\, M_{av}^2 + \frac{1}{2} M_{av}^4} \tag{44}$$

with

$$M_{av}^2 = M_a^2\, \sin^2\, \beta, \tag{45}$$

$$M_{bv}^2 = M_b^2 \sin^2 \alpha \tag{46}$$

and

$$\Delta L = L(T_a) - L(T_b). \tag{47}$$

The rest of the oblique shock relations for condensing flows can be written

$$\frac{\rho_b}{\rho_a} = \frac{(1 - \mu_m/\mu_v\, g^* + \gamma\, M_{bv}^2) M_{av}^2}{(1 - \mu_m/\mu_v\, g^* + \gamma\, M_{av}^2) M_{bv}^2}, \tag{48}$$

$$\frac{p_b}{p_a} = \frac{(1 - \mu_m/\mu_v\, g^* + \gamma\, M_{av}^2)}{(1 - \mu_m/\mu_v\, g^* + \gamma\, M_{bv}^2)}, \tag{49}$$

$$\frac{T_b}{T_a} = \frac{(1 - \mu_m/\mu_v\, g^* + \gamma\, M_{av}^2)^2\, M_{bv}^2}{(1 - \mu_m/\mu_v\, g^* + \gamma\, M_{bv}^2)^2\, M_{av}^2}, \tag{50}$$

$$\alpha = \tan^{-1}\left[\frac{(1 - \mu_m/\mu_v\, g^* + \gamma\, M_{av}^2)\, M_{bv}^2}{(1 - \mu_m/\mu_v\, g^* + \gamma\, M_{bv}^2)\, M_{av}^2} \tan \beta\right] \tag{51}$$

and

$$\varepsilon = \beta - \alpha. \tag{52}$$

It can further be shown that in the absence of condensation ($g^* = 0$), the relation between M_{bv}^2 and M_{av}^2, given by (43), yields the continuous solution $M_{av} = M_{bv}$ if the $(-)$ sign in front of the square root is chosen. Equation (43) reduces to the classical relation

$$M_{bv}^2 = \frac{2 + (\gamma - 1) M_{av}^2}{2\gamma\, M_{av}^2 - (\gamma - 1)} \tag{53}$$

if the $(+)$ sign in front of the square root is chosen. On the other hand, when $\beta = 90^\circ$, the oblique shock relations (43)–(52) reduce precisely to the normal shock relations for condensing flows.

Equations (43)–(52) permit implicit calculation of the flow variables behind the shock in terms of those ahead of the shock provided that one condition of the shock (usually chosen as the shock angle β) and the frozen condensate mass fraction g^* at the shock location are known. This will be achieved in the next section by introducing a novel shock fitting technique for embedded oblique shock waves. The solution given above by (43)–(52) is implicit since the latent heat L depends on temperature. When $\Delta L = 0$, the solution given by (43) with the $(-)$ sign chosen will correspond to the continuous solution, whereas the $(+)$ sign will yield an explicit discontinuous solution relating M_{bv}^2 to M_{av}^2. In this case the flow variables behind the shock can be written explicitly in terms of those ahead of the shock provided that the shock is properly located. When $\Delta L \neq 0$, both signs may yield discontinuous solutions which should be obtained by iteration starting with the condition $\Delta L = 0$. In general, embedded oblique shock waves encountered in condensing Prandtl–Meyer flows are weak so that the solution with $\Delta L \approx 0$ suffices for all practical purposes.

5. Shock fitting for embedded oblique shock waves

The oblique shock relations of the previous section need to be supplemented by a shock fitting technique which determines the shock location in the physical plane. In this section we introduce a shock fitting technique by satisfying the global conservation of mass across the shock for each streamtube of arbitrarily small cross-sectional area (this idea can also be found in Clarke & Delale 1988). Let S_1 and S_2 be

two streamlines of arbitrarily small normal separation intersecting the shock front, respectively, at points 1 and 2 as shown in figure 7. Across the oblique shock, the normalized oblique area, denoted by A_{obl} is continuous, but the normal area entering the continuity equation,

$$\rho\, u\, A = \text{constant} \tag{54}$$

along streamlines, is discontinuous. Using global conservation of mass for the streamtube formed by streamlines S_1 and S_2 of figure 7, we have

$$\rho_{1a}\, u_{1a}\, A_{1a} = \rho_{1b}\, u_{1b}\, A_{1b} \tag{55}$$

where, as usual, subscripts a and b denote, respectively, the flow properties just ahead and behind the shock front. In (55), A_{1a} is the normal area at point $1a$ (shown by the line 1–4 in figure 7) and A_{1b} is the normal area of the streamtube formed by the deflected streamlines passing through points $1b$ and $2b$ at the shock front and continued analytically upstream as if there were no shocks. From the geometry of figure 7, we have the relations

$$A_3 = A_{obl}\, \sin\alpha \tag{56}$$

and

$$A_{1a} = A_{obl}\, \sin(\beta + \Delta\beta) \tag{57}$$

where A_3 (shown by the line $2b$–3 in figure 7) is the normal area at point 3 of the streamtube, formed by the deflected streamlines passing through points $1b$ and $2b$, so that we have

$$\frac{\sin(\beta + \Delta\beta)}{\sin\alpha} = \frac{A_{1a}}{A_3} \tag{58}$$

where β is the shock angle at point 1 and $\beta + \Delta\beta$ is the shock angle at point 2. On the other hand, it follows from the area–direction relation

$$\frac{1}{A}\frac{\partial A}{\partial s} = -\frac{\partial\theta}{\partial n} \tag{59}$$

that

$$A_3 = A_{1b}\left[1 - \left(\frac{\partial\theta}{\partial n}\right)_{1b}\Delta s + O\left((\Delta s)^2\right)\right] \tag{60}$$

along the streamline downstream of the shock passing through point 1 with Δs denoting the projection of the shock front 1–2 onto the deflected streamline through point 1. Using the oblique shock relation (36) at point 1 together with (55), (58) and (60), we obtain

$$(\cot\beta)\,\Delta\beta = \left(\frac{\partial\theta}{\partial n}\right)_{1b}\Delta s \tag{61}$$

to linear approximations in $\Delta\beta$ and Δs. In the continuous or no-shock limit ($\varepsilon \to 0$), (61) reduces to

$$(\cot\mu)\,\delta\mu = \left(\frac{\partial\theta}{\partial n}\right)_{1a}\Delta s \tag{62}$$

where $\mu + \delta\mu$ is the Mach angle at point $2'$ in figure 7. The point $2'$ lies on the Mach line passing through point 1 and continued downstream of the shock without deflection, and the projection of the portion 1–$2'$ of this Mach line on the undeflected streamline through point 1 downstream of the shock is Δs. Let us consider the streamline passing through point $2'$ in the continuous or no-shock limit ($\varepsilon \to 0$), and

let $2''$ be the point on this streamline at the shock location where the continuous Mach angle is $\mu + \delta\mu''$. Now the difference in Mach angles between points $2'$ and $2''$ in figure 7, in the linear approximation, yields

$$\delta\mu'' - \delta\mu = \left(\frac{\partial\mu}{\partial s}\right)_{2''} \delta s \tag{63}$$

where δs is the length of the portion of the streamline between points $2'$ and $2''$. Similarly, the difference in Mach angles between points 2 and $2''$, in the linear approximation, can be written as

$$\Delta\mu - \delta\mu'' = \left(\frac{\partial\mu}{\partial\chi}\right)_{2} \delta\chi \tag{64}$$

where $\mu + \Delta\mu$ is the Mach angle at point 2 ahead of the shock and χ is the arcwise parameter characterizing the shock front with $\delta\chi$ being the distance between points 2 and $2''$. Consequently, we have

$$\Delta\mu = \delta\mu + \left(\frac{\partial\mu}{\partial s}\right)_{2''} \delta s + \left(\frac{\partial\mu}{\partial\chi}\right)_{2} \delta\chi \tag{65}$$

in the linear approximation. It can easily be shown that as $\varepsilon \to 0$, we have $\delta s \to 0$ and $\delta\chi \to 0$ with $\Delta s \neq 0$. For most of the embedded oblique shock waves, the angle of deflection ε of streamlines at the shock front is small compared to the shock angle β or Mach angle μ. For such shock waves both $\delta s/\Delta s$ and $\delta\chi/\Delta s$ are of $O(\varepsilon)$ or less and thus can be neglected with respect to unity (*the small deflection angle approximation*). Therefore, (62) can be written as

$$(\cot\,\mu)\,\Delta\mu = \left(\frac{\partial\theta}{\partial n}\right)_{1a} \Delta s \tag{66}$$

in the small deflection angle approximation. In this approximation it follows from (61) and (66) in the limit as $\Delta\mu \to 0$ that

$$\frac{\mathrm{d}\zeta}{\mathrm{d}\eta} = \frac{(\partial\theta/\partial n)_b}{(\partial\theta/\partial n)_a} \tag{67}$$

provided that $(\partial\theta/\partial n)_a \neq 0$ (or equivalently $\Delta\mu \neq 0$) at any point on the shock front where ζ and η are defined by

$$\zeta = \ln(\sin\beta) \tag{68}$$

and

$$\eta = \ln(\sin\mu). \tag{69}$$

It is essential to mention that the right-hand side of (67) would not only depend on the flow properties at a ahead of the shock and at b behind the shock, but also on β and $\mathrm{d}\beta/\mathrm{d}\mu$ (consequently, on η, ζ and $\mathrm{d}\zeta/\mathrm{d}\eta$) as well as on g^*. On the other hand, the flow properties at b behind the shock can be related to those ahead of the shock at a, to μ and β (thus to η and ζ) and to g^* using the oblique shock relations (43)–(52). Since $g^* \ll 1$ and varies insignificantly along the shock, the dependence of the right-hand side of (67) on g^* can be ignored. Consequently, the right-hand side of (67) can be taken as a function of η, ζ and $\mathrm{d}\zeta/\mathrm{d}\eta$ yielding a first-order ordinary differential equation for the parametric representation of ζ by η (or of the shock angle β by the Mach angle μ). It should also be mentioned that such a parametric representation fails if the flow just ahead of the shock is uniform (in such a case

parametric representation of the shock front has to be made by variables behind the shock). At the embedded shock origin, we have $\beta_K = \mu_K$ and $(\mathrm{d}\beta/\mathrm{d}\mu)_K = 1$. It then follows from the definitions (68) and (69) that $\zeta_K = \eta_K$ and $(\mathrm{d}\zeta/\mathrm{d}\eta)_K = 1$. Furthermore, at point K, we have $(\partial\theta/\partial n)_a = (\partial\theta/\partial n)_b$ so that, assuming that an analytical solution to (67) exists, we can approximate the right-hand side of (67) along the shock front KL of figure 1 by

$$\frac{(\partial\theta/\partial n)_b}{(\partial\theta/\partial n)_a} = 1 + 2\,C\,(\eta - \eta_K) \tag{70}$$

for $\eta \geqslant \eta_K$ where C is constant to be determined. In (70) we have assumed that $\eta - \eta_K = \ln M_K/M_g \ll 1$, where M_g is the flow Mach number and M_K its value at the embedded shock origin. This assumption corresponds to slowly varying flow Mach numbers along the shock front, which seems to be justified in the small deflection angle approximation and which is typical of most practical flow situations. Using the initial condition $\zeta_K = \eta_K$, (67)–(70) then yield the relation

$$\sin\beta = (\sin\mu)\exp\left[C\left(\ln\frac{\sin\mu}{\sin\mu_K}\right)^2\right] \tag{71}$$

for $\mu \geqslant \mu_K$. Since $\beta \geqslant \mu$, it follows from (71) that $C \geqslant 0$. It is important to mention that the function $\beta = \beta(\mu)$ is of class C^1, but not of class C^2 (see figure 8); therefore, the point K is a singularity where the function $\beta(\mu)$ and its first derivative $\mathrm{d}\beta/\mathrm{d}\mu$ are continuous, but not its second derivative $\mathrm{d}^2\beta/\mathrm{d}\mu^2$. In fact the second derivative $\mathrm{d}^2\beta/\mathrm{d}\mu^2$ at point K exhibits a discontinuity with a finite value defined by

$$\left(\frac{\mathrm{d}^2\beta}{\mathrm{d}\mu^2}\right)_K^+ \equiv \lim_{\mu\to\mu_K^+}\frac{\mathrm{d}^2\beta}{\mathrm{d}\mu^2} > 0 \tag{72}$$

as $\mu \to \mu_K^+$ and a vanishing value as $\mu \to \mu_K^-$ (see figure 8). The constant C in (71) can thus be related to this discontinuity by the relation

$$C = \frac{\tan\mu_K}{2}\left(\frac{\mathrm{d}^2\beta}{\mathrm{d}\mu^2}\right)_K^+ \tag{73}$$

so that (71) becomes

$$\sin\beta = (\sin\mu)\exp\left[\frac{\tan\mu_K}{2}\left(\frac{\mathrm{d}^2\beta}{\mathrm{d}\mu^2}\right)_K^+\left(\ln\frac{\sin\mu}{\sin\mu_K}\right)^2\right] \tag{74}$$

for $\mu \geqslant \mu_K$. It can also be shown (see Appendix A) that (74) reduces to the relation

$$\beta = \mu + \frac{1}{2}\left(\frac{\mathrm{d}^2\beta}{\mathrm{d}\mu^2}\right)_K^+(\mu - \mu_K)^2 \tag{75}$$

for $\mu > \mu_K$ near the vicinity of the embedded shock origin K. Equation (74) provides a fundamental relation for shock fitting between the shock angle β and the Mach angle μ along the shock front *in the small deflection angle approximation* ($\varepsilon \ll \beta$). The constant $(\mathrm{d}^2\beta/\mathrm{d}\mu^2)_K^+$, which appears in (74), arises from the singular behaviour of the embedded shock origin K and is, unfortunately, very difficult to estimate even for cases where the subcritical flow field in the immediate vicinity of point K can be calculated very accurately (recall the difficulties associated with the near-corner solution mentioned in § 3.3). In this paper we will vary this constant in an appropriate range to see how it affects the shock locations observed in experiments.

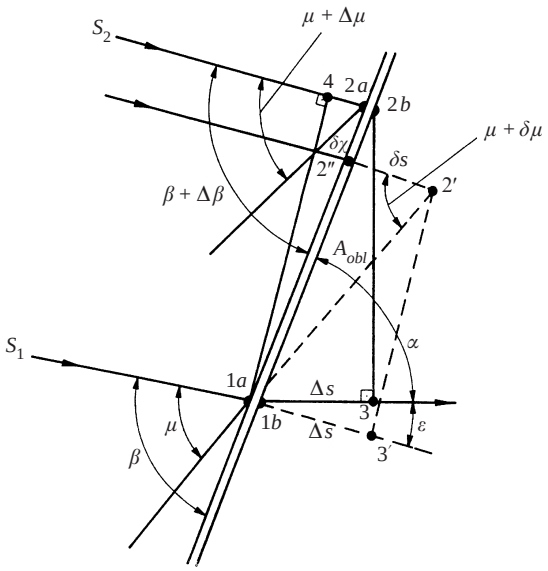

FIGURE 7. Geometry of an oblique shock wave for global mass conservation through a streamtube formed by two streamlines S_1 and S_2 (subscripts a and b denote, respectively, variables just ahead of and behind the shock front, μ and β are, respectively, the Mach angle and the shock angle at point 1 where streamline S_1 meets the shock front, $\mu + \Delta\mu$ and $\beta + \Delta\beta$ are, respectively, the Mach angle and the shock angle at point 2 where streamline S_2 meets the shock front, A_{obl} is the oblique area of the streamtube at the shock location, ε is the angle of deflection of streamline S_1 by the shock front and the dashed lines show the corresponding positions of the Mach lines and of the streamlines for flows without the shock).

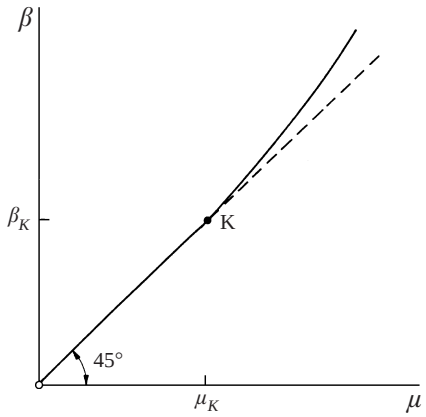

FIGURE 8. Relation of the shock angle β to the Mach angle μ ahead of the shock (K is the embedded shock origin and $\mu_K = \beta_K$ is the Mach angle at K).

6. Asymptotic solution of the flow field for supercritical Prandtl–Meyer flows

We are now ready to construct an algorithm for supercritical Prandtl–Meyer flows using the asymptotic solution of the condensation rate equation along streamlines. As mentioned earlier, for regions near the corner where the streamlines do not intersect the embedded shock front, the subcritical asymptotic solution of Part 1 applies as long as we are not in the immediate vicinity of the corner. For a discussion of the solution

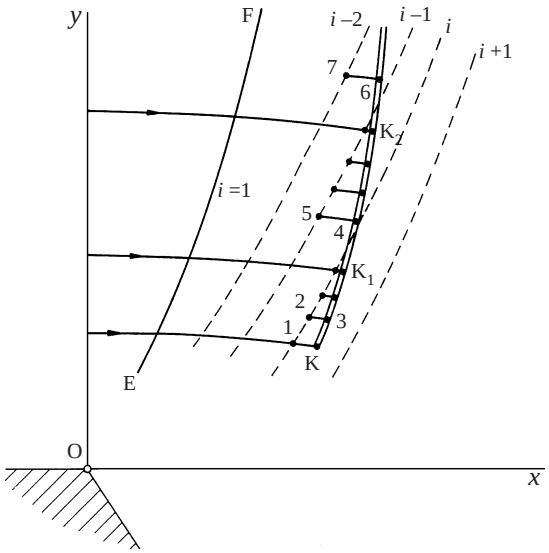

FIGURE 9. Construction of the embedded shock front in the heat addition zones (EF is the subcritical nucleation wave front and K is the embedded shock origin).

for the flow field in regions where streamlines meet the embedded shock front, first it is necessary to construct the embedded shock front. The coordinates of the embedded shock origin K can readily be obtained from the results of § 3. To proceed with the construction of the shock front by utilizing the shock fitting technique of the previous section, we first note that the shock front, which originates in the heat addition zones, may, depending on the amount of heat released, be directed towards the nearly frozen zones by condensation. In general, a portion KG of the embedded shock lies in the heat addition zones whereas the portion GL lies in the nearly frozen zones, as shown in figure 1. Therefore, it is essential to consider the construction of both portions.

6.1. *Construction of the embedded shock front in the heat addition zones*

For the construction of the shock front in the heat addition zones, we consider the subcritical asymptotic solution of Part 1 in these zones. Let the embedded shock origin K lie between the ith and $(i+1)$th shells of the network of characteristics for the solution algorithm of Part 1 in the heat addition zones, as shown in figure 9, and let EF denote the subcritical nucleation wave front. Consider the streamline passing through the embedded shock origin K and let point 1 denote the intersection point of this streamline with the ith shell and point 2 be next to point 1 on the ith shell where streamlines intersect the ith shell. Draw the line K3 with shock angle $\beta_K = \mu_K$ to obtain the initial portion of the shock which intersects the streamline passing through point 2 at point 3 (see figure 9). Evaluate the flow field at point 3 ahead of the shock and find the Mach angle μ_{3a} at that point. Now evaluate the shock angle β_3 from (74) of the previous section. Proceed in the same way to arrive eventually at point K_1 of figure 9 where the linear portion of the shock front originating from K_1 can no longer cross a streamline through a point on the ith shell. Now locate point 5 on the $(i-1)$th shell in such a way that the closest lower point to point 5 on the $(i-1)$th shell is on the streamline passing through point K_1. Construct the linear portion $K_1 4$ of the shock front, which intersects the streamline through point 5 at point 4. Evaluate the flow field at point 4 ahead of the shock front, particularly

the Mach angle μ_{4a}. Then find the shock angle β_4 from (74). Continue the above procedure until point K_2 is reached where further construction of the shock front crosses streamlines passing nearest through points on the $(i-2)$th shell. Proceed into the $(i-2)$th, $(i-3)$th, etc. shells until the first shell is met, i.e. the subcritical nucleation wave front EF, at point G (it is important to mention that sometimes, in regions of interest, the shock front does not need to meet the subcritical nucleation wave front; in such a case the shock front KL lies completely in the heat addition zones). The above algorithm completes the construction of the portion KG of the shock front in the heat addition zones provided that the embedded shock origin K lies on a streamline where the subcritical asymptotic solution remains valid, i.e. K does not lie too close to the corner. This latter case corresponds to strong heat addition near the corner; therefore, point G would also lie in the immediate vicinity of the corner and, thereby, of point K. It would then be difficult to predict the solution for the flow field therein using the subcritical asymptotic solution of Part 1 (see § 3.3). Fortunately, in such a case, one is usually interested in the solution in regions away from point K (or point G) where the shock front lies in the nearly frozen zones of Part 1. For these cases it is sufficient to predict only the coordinates of point G instead of the complete flow field of the heat addition zones in the immediate vicinity of the corner. In what follows we employ a shooting method based on the near-corner solution of § 3.3 for the prediction of the coordinates of point G. Assuming that the embedded shock origin lies on a characteristic given by (17), we can approximate the shock front by the parabola

$$y = D(x - x_K)^2 + B_K(x - x_K) + y_K \tag{76}$$

where the coordinates (x_K, y_K) of the embedded shock origin K are given by (30) and (31) and where B_K is defined by

$$B_K = 2A(m_K)[x_K - x_\ell(m_K)] + m_K \tag{77}$$

with m_K given by (29). Since G lies both on the shock front KG and on the subcritical nucleation wave front EF, it follows that the coordinates (x_G, y_G) of point G satisfy the relations

$$y_G = D\,[x_\ell(m_G) - x_K]^2 + B_K\,[x_\ell(m_G) - x_K] + y_K \tag{78}$$

and

$$y_G = m_G x_G = m_G x_\ell(m_G) \tag{79}$$

where m_G denotes the slope of the Mach line emanating from the corner on which G lies and where $x_G = x_\ell(m_G)$. Equations (78) and (79) provide two equations for the three unknowns y_G, m_G and D. The third relation between these unknowns follows by satisfying (74) for shock fitting at G which yields

$$\tan\beta_G = \frac{\exp\left[\tan\mu_K \left(\mathrm{d}^2\beta/\mathrm{d}\mu^2\right)_K^+ (\ln(M_G\sin\mu_K))^2/2\right]}{\left\{M_G^2 - \exp\left[\tan\mu_K \left(\mathrm{d}^2\beta/\mathrm{d}\mu^2\right)_K^+ (\ln(M_G\sin\mu_K))^2\right]\right\}^{1/2}} \tag{80}$$

where

$$M_G = M(m_G) = \left(1 + \left(\frac{\gamma+1}{\gamma-1}\right)\tan^2\left\{\left(\frac{\gamma-1}{\gamma+1}\right)^{1/2}\left[\omega(M_1) + \tan^{-1}\frac{1}{m_G}\right]\right\}\right)^{1/2} \tag{81}$$

with $\omega(M_1)$ denoting the Prandtl–Meyer function evaluated at the oncoming flow Mach number M_1. Equation (81) corresponds to the solution of the Mach number

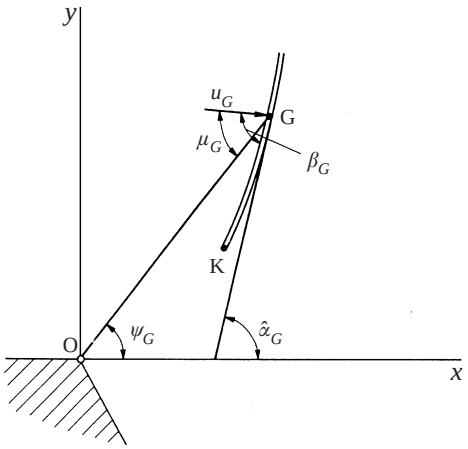

FIGURE 10. Estimation of point G, where the embedded shock front meets the subcritical nucleation wave front (μ_G and β_G are, respectively, the Mach angle and the shock angle at G, ψ_G is the inclination angle of the isentropic Mach line through G and $\hat{\alpha}_G$ is the inclination angle of the tangent to the shock front at G).

evaluated at point G as an explicit function of the similarity variable m_G worked out in detail in Appendix B (for the first time to the best knowledge of the authors). On the other hand, it follows from the geometry of figure 10 that

$$\hat{\alpha}_G - \psi_G = \beta_G - \mu_G \tag{82}$$

where $\tan \psi_G = m_G$ and $\hat{\alpha}_G$ is the angle between the line tangent to the shock front and the x-axis. From (78) and (79) we obtain

$$\tan \hat{\alpha}_G \equiv f(m_G) = 2\,\frac{m_G\, x_\ell(m_G) - y_K}{x_\ell(m_G) - x_K} - B_K. \tag{83}$$

By taking the tangent of both sides of (82) and by utilizing (83), one arrives at

$$\tan \beta_G = \frac{[f(m_G) - m_G](M_G^2 - 1)^{1/2} + m_G\, f(m_G) + 1}{[1 + m_G\, f(m_G)](M_G^2 - 1)^{1/2} + m_G - f(m_G)} \tag{84}$$

where $f(m_G)$ is given by (83) and $M_G = M(m_G)$ is given by (81). Equations (80) and (84) provide an equation for m_G for a given value of $(\mathrm{d}^2\beta/\mathrm{d}\mu^2)_K^+$. The coordinates of the point G are then given by

$$x_G = x_\ell(m_G) \quad \text{and} \quad y_G = m_G\, x_\ell(m_G). \tag{85}$$

The portion KG of the embedded shock front lying in the heat addition zones is given by (76) where the constant D can now be evaluated using (78) and (85).

6.2. *Construction of the embedded shock front in the nearly frozen zones*

When the shock front meets the subcritical nucleation front at point G, it extends nearly to the frozen zones. A method for obtaining the coordinates of the point G, when it lies close to the embedded shock origin K, has already been discussed in the previous section. Here we show that the construction of the portion GL of the shock front in the nearly frozen zones can be performed very accurately. In the nearly frozen zones the relation between the flow Mach number and the similarity variable m, i.e. the slope of a Mach line emanating from the corner, can be taken as the isentropic

relation

$$M = M(m) = \left(1 + \left(\frac{\gamma+1}{\gamma-1}\right) \tan^2 \left\{ \left(\frac{\gamma-1}{\gamma+1}\right)^{1/2} \left[\omega(M_1) + \tan^{-1} \frac{1}{m}\right] \right\}\right)^{1/2} \tag{86}$$

for $0 < \tan^{-1}(1/m) < \pi$ as worked out in detail in Appendix B (this relation follows from the solution of the Riemann invariant equation $\omega(M) - \theta = \omega(M_1)$ with ω denoting the classical Prandtl–Meyer function. To the best of our knowledge this explicit solution which relates the isentropic Mach number M to the similarity variable m is not available in the literature). It follows from the geometry of figure 11, where the portion GL of the shock front lies in the nearly frozen zones, that

$$\frac{\mathrm{d}y}{\mathrm{d}x} = \tan(\beta - \theta) = \frac{\tan\beta - \tan\theta}{1 + (\tan\beta)\tan\theta} \tag{87}$$

where

$$\tan\beta = f_1(m) = \frac{\exp\left[\tan\,\mu_K \left(\mathrm{d}^2\beta/\mathrm{d}\mu^2\right)_K^+ (\ln(M(m)\sin\mu_K))^2/2\right]}{\left\{M^2(m) - \exp\left[\tan\,\mu_K \left(\mathrm{d}^2\beta/\mathrm{d}\mu^2\right)_K^+ (\ln(M(m)\sin\mu_K))^2\right]\right\}^{1/2}} \tag{88}$$

and

$$\tan\theta = f_2(m) = \tan[\omega\{M(m)\} - \omega(M_1)] \tag{89}$$

with the similarity variable m given by $m = y/x$. Consequently, we obtain the homogeneous first-order differential equation

$$\frac{\mathrm{d}y}{\mathrm{d}x} = F\left(\frac{y}{x}\right) \tag{90}$$

for the shock front where the function $F(m)$ is defined by

$$F(m) = \frac{f_1(m) - f_2(m)}{1 + f_1(m) f_2(m)} \tag{91}$$

with $f_1(m)$ and $f_2(m)$ given, respectively, by (88) and (89). The solution to the initial value problem with initial values $x = x_G = x(m_G)$ and $y = y_G = m_G x_G$ yields the parametric equations for the shock front GL as

$$x = x(m) = x_G \exp\left[\int_{m_G}^{m} \frac{\mathrm{d}t}{H(t)}\right] \tag{92}$$

and

$$y = y(m) = m\,x_G \exp\left[\int_{m_G}^{m} \frac{\mathrm{d}t}{H(t)}\right] \tag{93}$$

for $m_G < m < \infty$ with the function $H(m)$ defined by

$$H(m) = F(m) - m. \tag{94}$$

Equations (92) and (93) yield the location of the embedded shock front in the nearly frozen zones on any Mach line with slope $m = \tan\psi$ and require only the evaluation of the integral in the argument of the exponential function, which has to be carried out numerically. In practice it would be more convenient to solve the initial value

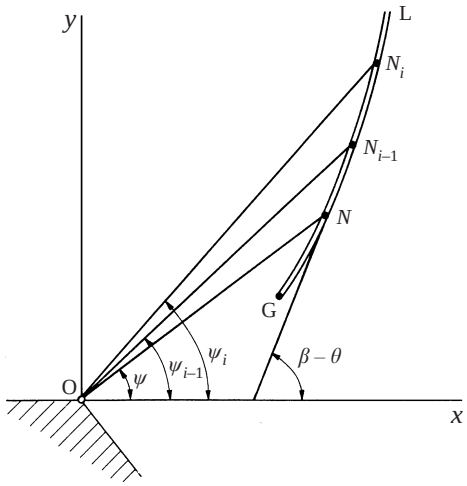

FIGURE 11. Construction of the portion GL of the embedded shock front in the nearly frozen zones (ψ is the angle of inclination of an isentropic Mach line, β is the shock angle and θ is the isentropic flow angle).

problem to the differential equation (87) using standard numerical techniques. For example, a simple Euler algorithm will yield the coordinates of the shock front on a Mach line with slope m_i as

$$x_i = \frac{\tan(\beta_{i-1} - \theta_{i-1}) - m_{i-1}}{\tan(\beta_{i-1} - \theta_{i-1}) - m_i}\, x_{i-1}, \quad i = 1, 2, 3, \ldots, \tag{95}$$

and

$$y_i = m_i x_i, \quad i = 1, 2, 3, \ldots, \tag{96}$$

starting with the Mach line through point G with initial value $x_0 = x_G$ at $m_0 = m_G$ and proceeding for arbitrarily small separation of slopes $m_i - m_{i-1}$, $i = 1, 2, \ldots$, (see figure 11).

6.3. *Construction of the network of characteristics downstream of the shock and supercritical flow solution*

Having completed the construction of the embedded shock front KL, with portion KG lying in the heat addition zones for shocks which extend to the nearly frozen zones, we first notice that the subcritical asymptotic solution of Part 1 applies along streamlines upstream of the shock front KL. The flow variables just behind the shock front then follow from the oblique shock relations (43)–(52). The construction of the network of characteristics downstream of the shock front KL and the flow solution therein need a separate consideration. We first consider the partition of points where streamlines intersect the shock front KL constructed by the method discussed in the previous sections. We order this partition of points by numbering them in the direction L to K as shown in figure 12. At this stage it is essential to distinguish between the asymptotic solutions of the condensation rate equation along the different classes of streamlines shown in figures 1 and 12. Naturally a considerable amount of heat is released along streamlines downstream of the embedded oblique shock front. For this reason it is essential to consider the characteristic form of the equations of motion in the heat addition zones:

$$\rho u\, \mathrm{d}u + \mathrm{d}p = 0, \tag{97}$$

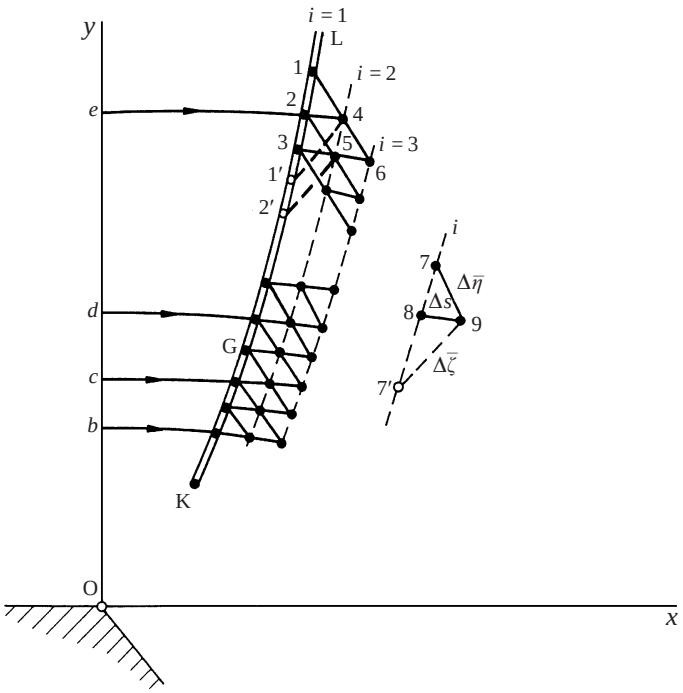

FIGURE 12. Construction of the network of characteristics downstream of the embedded shock front KGL (*b*, *c*, *d* and *e* are typical streamlines belonging to the different classes shown in figure 1).

$$h + \tfrac{1}{2}u^2 = c_{pm}\,T - \frac{\mu_m}{\mu_v}\,L(T)\,g + \tfrac{1}{2}u^2 = c_{pm} + \tfrac{1}{2}u_1^2, \tag{98}$$

$$u\,\mathrm{d}g - \varpi\,\mathrm{d}s = 0 \tag{99}$$

on streamlines, and

$$\sqrt{\frac{u^2}{a_f^2} - 1}\,\mathrm{d}p \pm \rho u^2\,\mathrm{d}\theta - \frac{h_g}{h_\rho}\,a_f\varpi \begin{pmatrix} \mathrm{d}\bar{\eta} \\ \mathrm{d}\bar{\zeta} \end{pmatrix} = 0 \tag{100}$$

on the characteristic lines

$$\frac{\mathrm{d}n}{\mathrm{d}s} = \mp\,\frac{1}{\sqrt{(u^2/a_f^2) - 1}}, \tag{101}$$

together with the thermal equation of state (5) valid everywhere (for details and definitions see (38)–(48) of Part 1; also, note that we have, respectively, used the symbols $\bar{\eta}$ and $\bar{\zeta}$ instead of η and ζ of Part 1 to avoid any confusion with the notation of § 5 of this paper). Consider the streamline through point 2, just behind the embedded oblique shock deflected by an angle ε_2 given by the shock relations, and the $\bar{\eta}$-characteristic through point 1 just behind the shock front as shown in figure 12. Let point 4 be their intersection point and 4–1′ be the $\bar{\zeta}$-characteristic through point 4 intersecting the shock front at point 1′ (see figure 12). Our aim is to locate points 4 and 1′, and to find the flow field at point 4 from the flow field at points 1, 2 and 1′ just behind the oblique shock front determined by the subcritical asymptotic solution of Part 1, the oblique shock relations and the shock construction discussed above. We first locate the coordinates of point 4 from (101) written for the characteristic line 1–4 and streamline 2–4 using the slopes at the initial shock front on the average. Point

$1'$ is then determined from (101) for the $1'$–4 characteristic using the slope at point $1'$ at the shock front as the average value for the slope (we can correct iteratively for the average value of the slopes after obtaining the flow field at point 4). We then write (97)–(99) on the streamline 2–4 through point 2, equation (100) with the $(-)$ sign chosen along the $\bar{\eta}$-characteristic 1–4 and with the $(+)$ sign chosen along the $\bar{\zeta}$-characteristic $1'$–4 together with the thermal equation of state (5) and the asymptotic solution along the streamline of appropriate class (class *e* in this case) downstream of the embedded oblique shock, as discussed in § 2, and solve for the flow field at point 4. We repeat this procedure for the streamline through point 3 at the shock front and for the $\bar{\eta}$-characteristic through point 2 to locate point 5 and the flow field therein. We continue this procedure along the shock front in the direction from L to K employing each time the asymptotic solution along the streamline of appropriate class downstream of the shock. We, thereby, obtain the points 4, 5, etc. as shown in figure 12, which we call the second ($i = 2$) shell, and the flow field at these points (by construction the first, $i = 1$, shell is the shock front and the flow field therein is known from the upstream solution, the oblique shock relations and shock construction). We repeat this procedure to obtain the third ($i = 3$), fourth ($i = 4$), etc. shells and the flow field at points constituting these shells (typical characteristic lines emerging from the *i*th shell for the construction of the next shell by the above procedure are shown in figure 12). We construct as many shells as necessary to approach equilibrium flow conditions in the droplet growth zones along streamlines downstream of the shock. Consequently, we obtain the supercritical flow field in regions of interest.

7. Condensation model and results

We are now in a position to calculate supercritical Prandtl–Meyer flow fields with homogeneous condensation by the method discussed above. We use the same condensation model as in Part 1, i.e. the classical nucleation rate equation and the Hertz–Knudsen droplet growth law. This model, with the poorly known surface tension and accommodation coefficients fitted to the experiments of Peters & Paikert (1989) by Schnerr & Dohrmann (1990), has proved successful for moist air expansions for a number of problems investigated (e.g. see Schnerr 1989; Delale *et al.* 1993*a*, *b*; Adam & Schnerr 1997) provided that the expansion rate is smaller than $3\,\mathrm{K}\,\mu\,\mathrm{s}^{-1}$ (see e.g. Delale & Schnerr 1996). Since this value for the expansion rate is exceeded on streamlines near the corner (the expansion rate at the corner is infinite), this condensation model is not valid in the neighbourhood of the corner (in this case unsteady effects of nucleation have to be considered). Consequently, we should employ this model only for computations in regions sufficiently far from the corner. The thermodynamic functions Σ, B, Ω and r^* together with the nucleation and droplet growth parameters K and λ, which appear in the normalized condensation rate equation (7), for this model are already given in Part 1.

Using the condensation model discussed above, an algorithm for supercritical Prandtl–Meyer flows can be developed for moist air expansions. The first step in the algorithm is the evaluation of the embedded shock origin by the shock formation theory of § 3. Here one has to distinguish between the two cases discussed in § 3 (for supercritical flows with appreciable heat addition, which will also be assumed here, the embedded shock origin lies on a characteristic emanating from the corner). Once the embedded shock origin is found, the embedded shock front is located utilizing the shock fitting technique of § 5 and the constructions given in §§ 6.1 and 6.2 together with an appropriate value for the constant $(\mathrm{d}^2\beta/\mathrm{d}\mu^2)_K^+$. The asymptotic

solution of Part 1 would then be valid along streamlines upstream of the oblique shock front and the application of the oblique shock relations of § 4 would yield the flow field just behind the embedded shock front. The asymptotic solution downstream of the embedded shock follows the guidelines of § 6.3. The most crucial point in this algorithm is the choice of the constant $(\mathrm{d}^2\beta/\mathrm{d}\mu^2)_K^+$. For this reason we propose a compatibility condition between the shock location and the value of the frozen condensate mass fraction g^* at the shock front, which needs to be satisfied at every point along the shock front. This compatibility condition can be stated as follows: *The frozen condensate mass fraction g^* at any point on the embedded shock front should be such that a substantial amount of heat must be released along streamlines in zones just downstream of the embedded shock front*. If this compatibility condition is violated anywhere on the shock front, we would conclude that the value chosen for the constant $(\mathrm{d}^2\beta/\mathrm{d}\mu^2)_K^+$ is not the appropriate value for shock fitting. The above compatibility condition can also be used to determine to what extent supercritical Prandtl–Meyer flows can be achieved in experiments designed for corner expansion flows with homogeneous condensation, recalling the difficulties in achieving such flows as discussed in Part 1. In this case we choose the constant $(\mathrm{d}^2\beta/\mathrm{d}\mu^2)_K^+$ so that experimental onset conditions lie on the shock front embedded in the nearly frozen zones. We evaluate the flow field using the algorithm constructed above for supercritical Prandtl–Meyer flows. We then check to what extent the compatibility condition is satisfied along the shock front.

We can now apply the above algorithm to the experiments of Smith (1971) for moist air expansions, which were shown to be supercritical in Part 1. Figure 13(*a*) shows the embedded shock origin K and the position of the embedded shock front KL for $(\mathrm{d}^2\beta/\mathrm{d}\mu^2)_K^+ = 0.01$ together with the nucleation wave front CF (obtained by extrapolation from the subcritical algorithm of Part 1) using the above supercritical algorithm for the experiments of Smith (1971) for supply temperature $T_0' = 284\,\mathrm{K}$, supply specific humidity $\omega_0 = 6.8\,\mathrm{g\,kg^{-1}}$ and supply relative humidity $\varphi_0 = 0.41$. Figure 13(*b*) shows the same characteristics for the experiments of Smith (1971), but with $(\mathrm{d}^2\beta/\mathrm{d}\mu^2)_K^+ = 1.8$ for supply temperature $T_0' = 284\,\mathrm{K}$, supply specific humidity $\omega_0 = 6.4\,\mathrm{g\,kg^{-1}}$ and supply relative humidity $\varphi_0 = 0.69$. Comparison of these figures shows that the increase in relative humidity shifts the embedded shock origin K, and consequently point G, closer to the corner, signifying stronger heat release by condensation. Figure 14(*a*) shows the positions of the shock front KL_1 for $(\mathrm{d}^2\beta/\mathrm{d}\mu^2)_K^+ = 0.01$ and of KL_2 for $(\mathrm{d}^2\beta/\mathrm{d}\mu^2)_K^+ = 1.0$ together with the subcritical nucleation wave front CF for the experiments of Smith for the supply conditions stated in figure 13(*a*). In this case no significant change in the location of the point G is observed for the indicated values of the constant $(\mathrm{d}^2\beta/\mathrm{d}\mu^2)_K^+$. The best agreement with the experiments seems to be achieved by the curve KL_1 with a value of $(\mathrm{d}^2\beta/\mathrm{d}\mu^2)_K^+ = 0.01$.

Figure 14(*b*) shows the positions of the shock front KL_1 for $(\mathrm{d}^2\beta/\mathrm{d}\mu^2)_K^+ = 1.8$ and of KL_2 for $(\mathrm{d}^2\beta/\mathrm{d}\mu^2)_K^+ = 1.0$ together with the subcritical nucleation wave front CF for the experiments of Smith for the supply conditions in figure 13(*b*). In this case one can observe a shift in the location of point G for different values of $(\mathrm{d}^2\beta/\mathrm{d}\mu^2)_K^+$ (points G_1 and G_2 in the figure). The embedded shock front KL_1 obtained with $(\mathrm{d}^2\beta/\mathrm{d}\mu^2)_K^+ = 1.8$ seems to yield the best agreement with the experiments of Smith in this case. The remarkably good agreement of the embedded shock fronts KL_1 in figures 14(*a*) and 14(*b*) obtained by the shock fitting technique of § 5 demonstrates the success of this technique. From the construction of the embedded shock fronts KL_1 in figures 14(*a*) and 14(*b*), we find that the condensate mass fraction g^* varies slowly

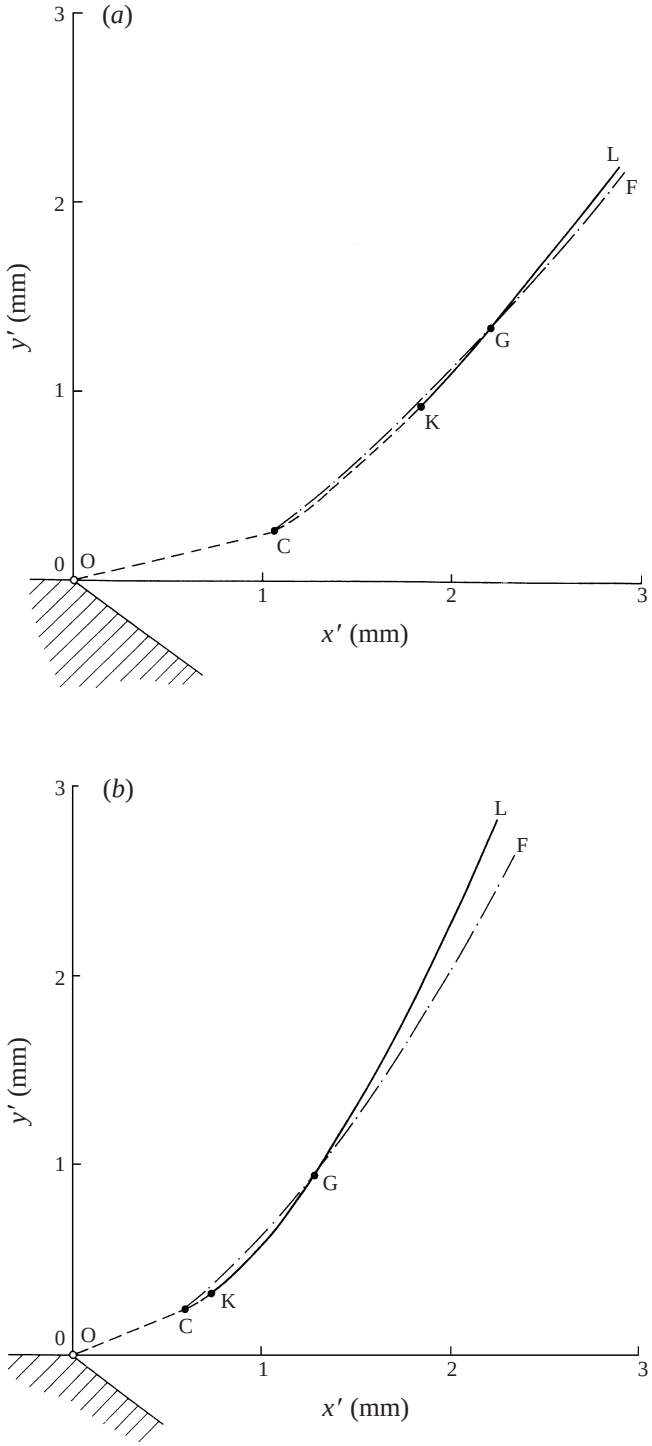

FIGURE 13. (*a*) The initial formation of the embedded shock front KGL, for $(\mathrm{d}^2\beta/\mathrm{d}\mu^2)_K^+ = 0.01$, and the subcritical nucleation wave front CGF for the experiments of Smith (1971) for nozzle supply temperature $T_0' = 284\,\mathrm{K}$, supply specific humidity $\omega_0 = 6.8\,\mathrm{g\,kg^{-1}}$ and supply relative humidity $\varphi_0 = 0.41$. (*b*) As (*a*) but for $(\mathrm{d}^2\beta/\mathrm{d}\mu^2)_K^+ = 1.8$, and supply specific humidity $\omega_0 = 6.4\,\mathrm{g\,kg^{-1}}$ and supply relative humidity $\varphi_0 = 0.69$.

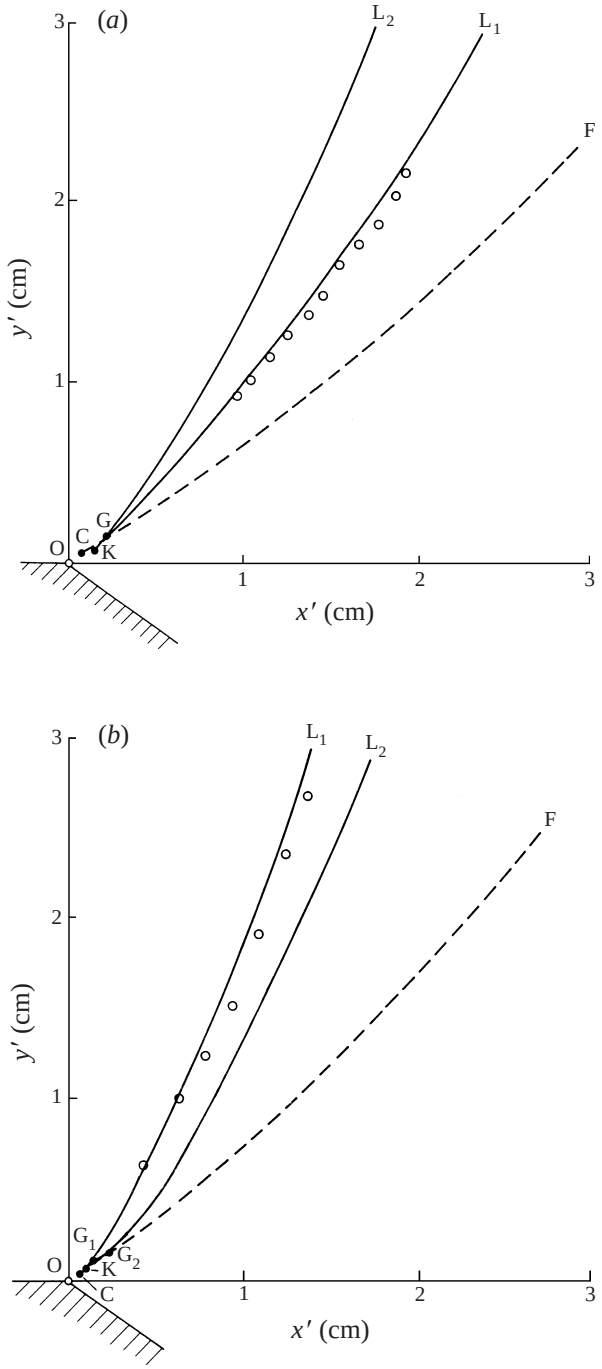

FIGURE 14. The embedded shock fronts KGL_1 and KGL_2, evaluated, respectively, for $(d^2\beta/d\mu^2)_K^+ = 0.01$ and 1.0, for the experiments of Smith (1971) for nozzle supply temperature $T_0' = 284\,K$, supply specific humidity $\omega_0 = 6.8\,g\,kg^{-1}$ and supply relative humidity $\varphi_0 = 0.41$ (○ denotes the experimental onset conditions and CGF is the subcritical nucleation wave front). (*b*) As (*a*) but for the embedded shock fronts KG_1L_1 and KG_2L_2, evaluated, respectively, for $(d^2\beta/d\mu^2)_K^+ = 1.8$ and 1.0, for supply specific humidity $\omega_0 = 6.4\,g\,kg^{-1}$ and supply relative humidity $\varphi_0 = 0.69$ (○ denotes the experimental onset conditions and CG_1G_2F is the subcritical nucleation wave front).

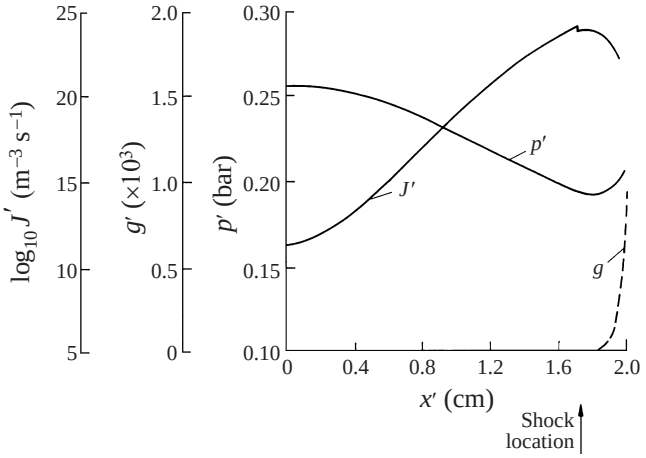

FIGURE 15. The distributions of the pressure p', the nucleation rate J' and the condensate mass fraction g along a streamline at initial distance $D' = 2.064$ cm from the corner for the experiments of Smith (1971) for nozzle supply temperature $T_0' = 284$ K, supply specific humidity $\omega_0 = 6.8\,\mathrm{g\,kg^{-1}}$ and supply relative humidity $\varphi_0 = 0.41$.

along the shock fronts with values between 1.3×10^{-6} and 8.5×10^{-6} along the shock front GL_1 of figure 14(*a*) and with values between 1.0×10^{-7} and 2.5×10^{-7} along the shock front G_1L_1 of figure 14(*b*), with the greater value as we get closer to the corner along the shock fronts. From the oblique shock relations of § 4, we find that the deflection angle ε (in radians) is of $O(10^{-4})$ along the shock front GL_1 of figure 14(*a*) and of $O(10^{-2})$ along the shock front G_1L_1 of figure 14(*b*), verifying the validity of the small deflection angle approximation used in § 5. The use of the oblique shock relations also shows that both shock fronts are weak, demonstrating the alternative possibility of employing the weak shock approximation of Whitham (1956, 1974) (e.g. the change in the flow Mach number ΔM across the shock fronts GL_1 of figure 14(*a*) and G_1L_1 of figure 14(*b*) is, respectively, of $O(10^{-4})$ and of $O(10^{-2})$). These quantitative results are also in agreement with those of the qualitative theory by Delale & van Dongen (1998) that only weak embedded shock waves can be observed in Prandtl–Meyer flows with non-equilibrium condensation.

We now consider the flow field downstream of the embedded shock front KL_1 (GL_1 in figure 14(*a*) and G_1L_1 in figure 14(*b*)) using the supercritical asymptotic algorithm discussed in detail in § 6.3. We first discuss the supercritical solution downstream of the embedded shock GL_1 of figure 14(*a*) (with $(\mathrm{d}^2\beta/\mathrm{d}\mu^2)_K^+$ chosen such that it almost coincides with the onset conditions in the experiments of Smith). Figure 15 shows the distributions of the pressure p', the nucleation rate J' and the condensate mass fraction g along a streamline at initial distance $D' = 2.064$ cm from the corner for the supply conditions given in figure 13(*a*) using the supercritical asymptotic solution downstream of the embedded shock front GL_1 of figure 14(*a*). The corresponding distributions for the flow Mach number M_g and for the temperature T' along the same streamline and for the same supply conditions are exhibited in figure 16. The results imply that a delay in appreciable latent heat addition occurs downstream of the embedded shock front, demonstrating the fact that the compatibility condition, mentioned above, between the value of the condensate mass fraction g^* (here of $O(10^{-6})$) and the embedded shock location is not satisfactorily reached for this case. Since the embedded shock front, fitted by the method of § 5, is at the experimentally

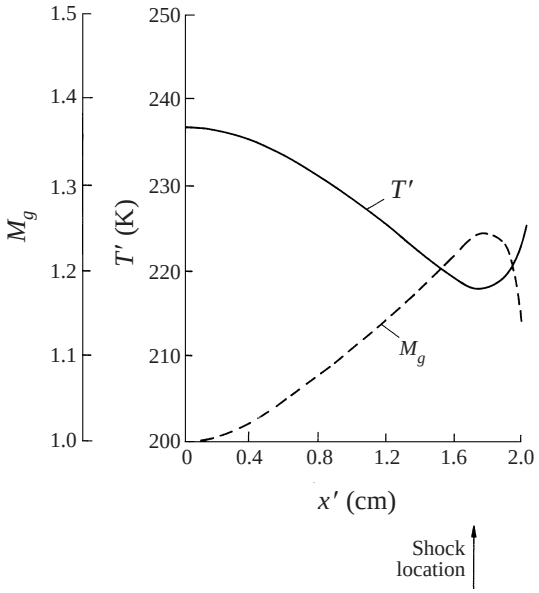

FIGURE 16. The distributions of the flow Mach number M_g and the temperature T' along a streamline with initial distance $D' = 2.064$ cm from the corner for the experiments of Smith (1971) for the supply conditions of figure 15.

observed location, we deduce that the value of the condensate mass fraction g^* at the shock location (obtained by the subcritical algorithm of Part 1) is not sufficiently large for considerable heat to be released in zones immediately following the shock front.

This incompatibility between g^* and the embedded shock location originates from the use of uniform velocity and non-nucleating conditions at the throat for the oncoming flow in Prandtl–Meyer flows in contrast to the nozzle flow conditions at the throat in the experiments of Smith (1971), a fact that has already been discussed in Part 1. Consequently, the flow field along the streamline at initial distance $D' = 2.064$ cm from the corner for the supply conditions given in figure 13(a) for the experiments of Smith (1971) resembles more closely that of flows in ducts and nozzles (see e.g. Schnerr 1987; Delale *et al.* 1993*b*) than that of supercritical Prandtl–Meyer flows exhibited in figures 15 and 16. Figure 17 shows the distributions of the pressure p', the nucleation rate J' and the condensate mass fraction g along a streamline for the same supply conditions as figure 15, but with initial distance $D' = 1.066$ cm from the corner. The corresponding distributions for the flow Mach number M_g and for the temperature T' along the same streamline and for the same supply conditions are exhibited in figure 18. The agreement between g^* (now of $O(10^{-5})$) and the shock location is better now despite the delay (here smaller) in the heat release downstream of the embedded shock front. Therefore, the flow field for the supply conditions given in figure 13 in the experiments of Smith approaches that for supercritical Prandtl–Meyer flows only along those streamlines lying sufficiently close to the corner. The flow deviates from the supercritical Prandtl–Meyer flows along streamlines far from the corner. The situation becomes worse for the supply conditions of figure 13(b) in the experiments of Smith (1971). In this case the flow is more or less frozen for long distances along streamlines (except for those very near the corner where it is difficult to obtain the solution) downstream of the shock front $G_1 L_1$ violating the compatibility condition. This shock wave lies very close to the throat of the nozzle

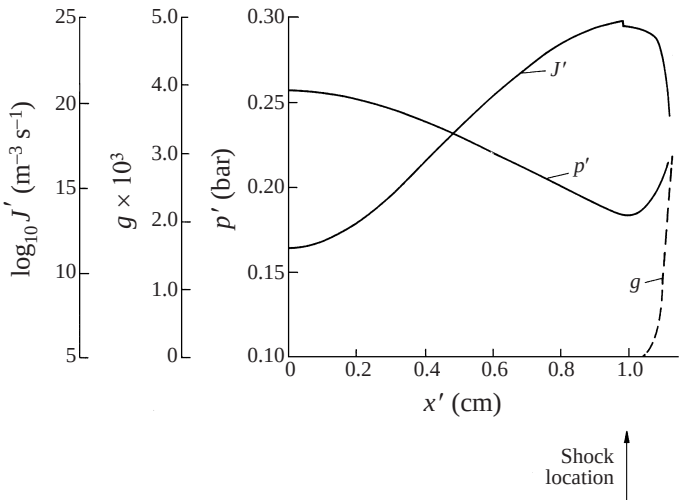

FIGURE 17. The distributions of the pressure p', the nucleation rate J' and the condensate mass fraction g along a streamline at initial distance $D' = 1.066$ cm from the corner for the experiments of Smith (1971) for the supply conditions of figure 15.

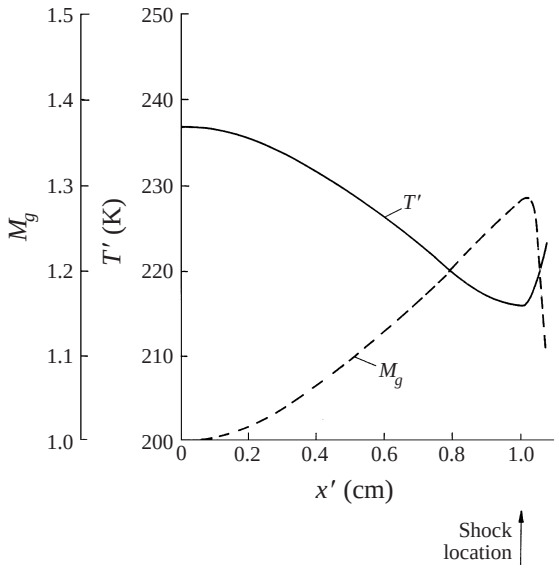

FIGURE 18. The distributions of the flow Mach number M_g and the temperature T' along a streamline at initial distance $D' = 1.066$ cm from the corner for the experiments of Smith (1971) for the supply conditions of figure 15.

in Smith's experiments and seems to represent the strong shock wave encountered in supercritical nozzle or duct flows with a downstream subsonic field (for experimental evidence of this in corner expansion flows, see Frank 1985).

8. Conclusions

Prandtl–Meyer flows with embedded oblique shock waves (supercritical flows) due to excessive heat release from condensation are considered using the asymptotic

solution of the condensation rate equation along streamlines. The necessary and sufficient conditions for the existence of embedded shock waves are given in the parabolic approximation of the equations of characteristics in the heat addition zones. The embedded shock origin is then located by the envelope construction of the family of characteristics in this approximation. A shock fitting technique for embedded oblique shock waves, containing a constant determined by a compatibility condition, is introduced in the small deflection angle approximation. Consequently, the law of deflection of a streamline through an embedded oblique shock wave is established in the same approximation. An algorithm for the flow field downstream of the embedded oblique shock wave in supercritical Prandtl–Meyer flows is constructed using the characteristic form of the equations of motion together with the asymptotic solution of the condensation rate equation along streamlines. The theory is then applied to the corner expansion flows in the experiments of Smith (1971), which have already been shown to be supercritical in Part 1. The results show that embedded shock waves close to the throat of the nozzle, where the corner is located, are strong shock waves with a subsonic flow field downstream, violating the compatibility condition between the embedded shock location and the value of the condensate mass fraction therein. Embedded shock waves considerably downstream of the throat and near the corner with higher Mach numbers, for which the compatibility between the shock location and the condensate mass fraction therein is satisfied, show features that are more or less characteristic of supercritical Prandtl–Meyer flows with homogeneous condensation. These features can be summarized as:

(*a*) subcritical flows can be observed only in regions in the immediate neighbourhood of the corner;

(*b*) the embedded shock origin, generally, lies on a characteristic emanating from the corner;

(*c*) the embedded shock waves observed are oblique and weak with small deflection angles, verifying the small deflection approximation for shock fitting;

(*d*) the embedded shock front is concave with respect to the oncoming flow;

(*e*) an increase in the supply relative humidity, with the rest of the supply conditions held fixed, shifts the embedded shock origin closer to the corner and the embedded shock front further upstream in the expansion fan;

(*f*) the flow field along streamlines upstream of the embedded shock front is nearly frozen, except within the thin onset zone, and considerable heat addition proceeds immediately along streamlines downstream of the shock front; and

(*g*) the overall thickness of the heat addition zones along streamlines downstream of the embedded shock front increases as the initial distance of the streamlines from the corner is increased.

Supercritical Prandtl–Meyer flows with homogeneous condensation seem difficult to be realized in experiments; therefore, they usually occur locally, as in the experiments of Smith (1971), where the asymptotic theory developed above yields satisfactory results.

C. F. D. is grateful to the University of Cambridge for their kind support that made his visit to the Department of Applied Mathematics and Theoretical Physics during Autumn 1998 possible. This work is also supported in part by the Scientific and Technical Research Council of Turkey (TÜBİTAK) and by the Turkish Academy of Sciences (TÜBA). The authors are grateful to Professor J. B. Young, Professor A. Kluwick, Professor G. H. Schnerr, Professor J. Zierep and Professor M. E. H. van

Dongen for many valuable comments. In particular, Professor M. E. H. van Dongen clarified the dependence of the right-hand side of (67).

Appendix A. Verification of (74) near the embedded shock origin

Consider the relation between the shock angle β and the Mach angle μ in the immediate neighbourhood of the embedded shock origin. At the embedded shock origin K, we have $\beta_K = \mu_K$ and $(\mathrm{d}\beta/\mathrm{d}\mu)_K = 1$. We also have $\beta = \mu$ for $\mu \leqslant \mu_K$ on the characteristic line where the embedded shock origin K is located. Combining this with (75) for $\mu > \mu_K$ we can write

$$\beta = \mu + \frac{1}{2}\left(\frac{\mathrm{d}^2\beta}{\mathrm{d}\mu^2}\right)_K^+ (\mu - \mu_K)^2\, \Theta(\mu - \mu_K) \tag{A 1}$$

for sufficiently small $(\mu - \mu_K)$ where Θ denotes the Heaviside unit step function. We now verify this law using (74). To do so, we evaluate the left-hand side of (74) using relation (A 1) and show that this is the same as the right-hand side of (74) in the vicinity of the embedded shock origin K. On employing relation (A 1) the left-hand side of (74) becomes

$$\text{L.H.S.} \equiv \frac{\sin\beta}{\sin\mu} = 1 + (\cot\mu)\, k^2 + O(k^4) \tag{A 2}$$

for $\mu > \mu_K$ where k is a small parameter ($k \ll 1$) defined by

$$k \equiv \left[\frac{1}{2}\left(\frac{\mathrm{d}^2\beta}{\mathrm{d}\mu^2}\right)_K^+\right]^{1/2} (\mu - \mu_K) > 0. \tag{A 3}$$

By expanding $\cot\mu$ for $\mu > \mu_K$ in powers of $(\mu - \mu_K)$ we obtain

$$\cot\mu = \cot\mu_K - \left[\frac{2}{(\mathrm{d}^2\beta/\mathrm{d}\mu^2)_K^+}\right]^{1/2} (1 + \cot^2\mu_K)\, k + O(k^2). \tag{A 4}$$

Using this equation together with (A 2) we arrive at

$$\text{L.H.S.} = 1 + (\cot\mu_K)k^2 - \left[\frac{2}{(\mathrm{d}^2\beta/\mathrm{d}\mu^2)_K^+}\right]^{1/2} (1 + \cot^2\mu_K)\, k^3 + O(k^4) \tag{A 5}$$

for $\mu > \mu_K$. Now we evaluate the right-hand side of (74) for $\mu > \mu_K$. By expanding in powers of $(\mu - \mu_K)$ one can show that

$$\frac{\sin\mu}{\sin\mu_K} = 1 + \left[\frac{2}{(\mathrm{d}^2\beta/\mathrm{d}\mu^2)_K^+}\right]^{1/2} (\cot\mu_K)k - \frac{1}{(\mathrm{d}^2\beta/\mathrm{d}\mu^2)_K^+}k^2 + O(k^3) \tag{A 6}$$

and

$$\ln\frac{\sin\mu}{\sin\mu_K} = \left[\frac{2}{(\mathrm{d}^2\beta/\mathrm{d}\mu^2)_K^+}\right]^{1/2} (\cot\mu_K)\, k - \frac{(1 + \cot^2\mu_K)}{(\mathrm{d}^2\beta/\mathrm{d}\mu^2)_K^+}\, k^2 + O(k^3). \tag{A 7}$$

We can now write

$$\frac{\tan\mu_K}{2}\left(\frac{\mathrm{d}^2\beta}{\mathrm{d}\mu^2}\right)_K^+ \left(\ln\frac{\sin\mu}{\sin\mu_K}\right)^2 = (\cot\mu_K)\, k^2 - \left[\frac{2}{(\mathrm{d}^2\beta/\mathrm{d}\mu^2)_K^+}\right]^{1/2} (1 + \cot^2\mu_K)\, k^3 + O(k^4). \tag{A 8}$$

Taking the exponential of (A 8) we obtain for $\mu > \mu_K$ the right-hand side of (74) as

$$\text{R.H.S.} = \exp\left[\frac{\tan\mu_K}{2}\left(\frac{\mathrm{d}^2\beta}{\mathrm{d}\mu^2}\right)_K^+\left(\ln\frac{\sin\mu}{\sin\mu_K}\right)^2\right]$$
$$= 1 + (\cot\mu_K)k^2 - \left[\frac{2}{(\mathrm{d}^2\beta/\mathrm{d}\mu^2)_K^+}\right]^{1/2}(1+\cot^2\mu_K)k^3 + O(k^4). \quad \text{(A 9)}$$

The left-hand side evaluated using (A 1) agrees with the right-hand side for sufficiently small k up to $O(k^4)$ verifying that (74) yields precisely the same results as (A 1) near the embedded shock origin K.

Appendix B. Solution of the Riemann invariant for the Mach number as a function of the similarity variable in isentropic Prandtl–Meyer flows

Consider the Riemann invariant

$$\theta = \mu - \psi = \omega(M) - \omega(M_1) \quad \text{(B 1)}$$

valid everywhere in the expansion fan of isentropic Prandtl–Meyer flows where $\omega(M)$ denotes the classical Prandtl–Meyer function defined by

$$\omega(M) = \left(\frac{\gamma+1}{\gamma-1}\right)^{1/2}\tan^{-1}\left[\frac{(\gamma-1)}{(\gamma+1)}(M^2-1)\right]^{1/2} - \tan^{-1}(M^2-1)^{1/2} \quad \text{(B 2)}$$

(for notation and details see Part 1). By taking the tangent of both sides of (B 1), one can write

$$\frac{1-mv}{v+m} = \tan[\kappa(v) - \tan^{-1}v] \quad \text{(B 3)}$$

where $m = \tan\psi$ is the similarity variable that denotes the slope of any particular Mach line in the expansion fan of isentropic Prandtl–Meyer flows and where v and $\kappa(v)$ are defined by

$$v = (M^2-1)^{1/2} \quad \text{(B 4)}$$

and

$$\kappa(v) = \left(\frac{\gamma+1}{\gamma-1}\right)^{1/2}\tan^{-1}\left[\left(\frac{\gamma-1}{\gamma+1}\right)^{1/2}v\right] - \omega(M_1). \quad \text{(B 5)}$$

By expanding the tangent in (B 3), one arrives at the relation

$$\tan\kappa(v] = 1/m. \quad \text{(B 6)}$$

Now by solving (B 5) and (B 6) for v as a function of the similarity variable m and using (B 4), we obtain the remarkable result

$$M = M(m) = \left(1 + \left(\frac{\gamma+1}{\gamma-1}\right)\tan^2\left\{\left(\frac{\gamma-1}{\gamma+1}\right)^{1/2}\left[\omega(M_1) + \tan^{-1}1/m\right]\right\}\right)^{1/2} \quad \text{(B 7)}$$

for $0 < \tan^{-1}(1/m) < \pi$. Equation (B 7) yields explicitly the isentropic Mach number on any Mach line with slope m in Prandtl–Meyer flows. The rest of the flow variables on the Mach line with slope m then follow from their relations to the Mach number.

REFERENCES

Adam, S. & Schnerr, G. H. 1997 Instabilities and bifurcation of non-equilibrium two-phase flows. *J. Fluid Mech.* **348**, 1–28.

Clarke, J. H. & Delale, C. F. 1988 Expansion flows on walls with nonequilibrium condensation. *Q. Appl. Maths* **XLVI**, 121–143.

Delale, C. F. & Crighton, D. G. 1998 Prandtl–Meyer flows with homogeneous condensation. Part 1. Subcritical flows. *J. Fluid Mech.* **359**, 23–47.

Delale, C. F. & Dongen, M. E. H. van 1998 Thermal choking in two-dimensional expansion flows. *Z. Angew. Math. Phys.* **49**, 515–537.

Delale, C. F. & Schnerr, G. H. 1996 Transient effects of nucleation in steady and unsteady condensing flows. *Intl J. Multiphase Flow* **22**, 767–781.

Delale, C. F., Schnerr, G. H. & Zierep, J. 1993*a* Asymptotic solution of transonic nozzle flows with homogeneous condensation. I. Subcritical flows. *Phys. Fluids* A **5**, 2969–2981.

Delale, C. F., Schnerr, G. H. & Zierep, J. 1993*b* Asymptotic solution of transonic nozzle flows with homogeneous condensation. II. Supercritical flows. *Phys. Fluids* A **5**, 2982–2995.

Frank, W. 1979 Prandtl–Meyer Expansion mit Wärmezufuhr. *Z. Angew. Math. Mech.* **59**, 223–226.

Frank, W. 1985 Condensation phenomena in supersonic nozzles. *Acta Mechanica* **54**, 135–156.

Kurshakov, A. V., Saltanov, G. A. & Tkalenko, R. A. 1971 Theoretical and experimental investigation of condensation in a centered rarefaction wave. *Prikl. Mech. Tekn. Phys.* **5**, 117.

Peters, F. & Paikert, B. 1989 Nucleation and growth rates of homogeneously condensing water vapor in argon from shock tube experiments. *Exps. Fluids* **7**, 521–530.

Schnerr, G. 1989 2-D transonic flow with energy supply by homogeneous condensation: Onset condition and 2-D structure of steady Laval nozzle flow. *Exps. Fluids* **7**, 145–156.

Schnerr, G. H. & Dohrmann, U. 1990 Transonic flow around airfoils with relaxation and energy supply by homogeneous condensation. *AIAA J.* **89**, 1187–1193.

Smith, L. T. 1971 Experimental investigation of the expansion of moist air around a sharp corner. *AIAA J.* **9**, 2035–2037.

Whitham, G. H. 1956 On the propagation of weak shock waves. *J. Fluid Mech.* **1**, 290–318.

Whitham, G. H. 1974 *Linear and Nonlinear Waves*, Chapter 9. Wiley.